



HAL
open science

Geomorphological Map of the Soi Crater Region on Titan

A. Schoenfeld, A. Solomonidou, M. Malaska, R. Lopes, S. Birch, Stéphane Le Mouélic, M. Florence, T. Verlander, S. Wall, C. Elachi

► **To cite this version:**

A. Schoenfeld, A. Solomonidou, M. Malaska, R. Lopes, S. Birch, et al.. Geomorphological Map of the Soi Crater Region on Titan. *Journal of Geophysical Research. Planets*, 2023, 128 (1), 10.1029/2022JE007499 . hal-03932607

HAL Id: hal-03932607

<https://hal.science/hal-03932607>







Submitted on 8 Dec 2023

HAL is a multi-disciplinary open access archive for the deposit and dissemination of scientific research documents, whether they are published or not. The documents may come from teaching and research institutions in France or abroad, or from public or private research centers.

L'archive ouverte pluridisciplinaire **HAL**, est destinée au dépôt et à la diffusion de documents scientifiques de niveau recherche, publiés ou non, émanant des établissements d'enseignement et de recherche français ou étrangers, des laboratoires publics ou privés.

Copyright

Geomorphological Map of the Soi Crater Region on Titan

A. M. Schoenfeld¹ , A. Solomonidou^{2,3,4} , M. J. Malaska⁵ , R. M. C. Lopes⁵ , S. P. D. Birch⁶,
S. Le Mouélic⁷ , M. Florence⁵ , T. Verlander⁸, S. D. Wall³, and
C. Elachi³

Key Points:

- Units are described in greater detail as part of the evolving Titan geomorphology mapping schema
- Empty lakes may reach latitudes as equatorial as 40°N on Titan
- The Soi crater region is consistent with the narrative of Titan's equatorial and mid-latitudes being dominated by organic depositional materials

Supporting Information:

Supporting Information may be found in the online version of this article.

Correspondence to:

A. M. Schoenfeld,
ashley.schoenfeld@ucla.edu

Citation:

Schoenfeld, A. M., Solomonidou, A., Malaska, M. J., Lopes, R. M. C., Birch, S. P. D., Le Mouélic, S., et al. (2023). Geomorphological map of the Soi crater region on Titan. *Journal of Geophysical Research: Planets*, 128, e2022JE007499. <https://doi.org/10.1029/2022JE007499>

Received 19 AUG 2022
Accepted 21 NOV 2022

¹Department of Earth, Planetary, and Space Sciences, University of California, Los Angeles, Los Angeles, CA, USA, ²Hellenic Space Center, Athens, Greece, ³California Institute of Technology, Pasadena, CA, USA, ⁴Faculty of Environmental Sciences, Czech University of Life Sciences Prague, Praha, Czech Republic, ⁵Jet Propulsion Laboratory, California Institute of Technology, Pasadena, CA, USA, ⁶Department of Earth, Atmospheric, and Planetary Science, Massachusetts Institute of Technology, Cambridge, MA, USA, ⁷Laboratoire Planétologie et Géosciences, Nantes Université, Université Angers, CNRS UMR 6112, Nantes, France, ⁸School of Civil Engineering and Environmental Science, University of Oklahoma, Norman, OK, USA

Abstract We mapped the Soi crater region at 1:800,000 scale and produced a geomorphological map using methodology presented by Malaska, Lopes, Williams, et al. (2016), <https://doi.org/10.1016/j.icarus.2016.02.021> and Schoenfeld et al. (2021), <https://doi.org/10.1016/j.icarus.2021.114516>. This region spans longitude 110° to 180°W and latitude 0° to 60°N and is representative of the transition between the equatorial, mid-latitude, and high-latitude northern regions of Titan. We used Cassini Synthetic Aperture Radar (SAR) as our primary mapping data set. For areas where SAR was not available, we used lower resolution data from the Imaging Science Subsystem, the Visible and Infrared Mapping Spectrometer, radiometry, and high-altitude SAR for complete mapping coverage of the region. We identified 22 geomorphological units, 3 of which have been discussed in existing literature but have not yet been incorporated into our mapping investigations. These include sharp-edged depressions (*bse*), ramparts (*brh*), and bright gradational plains (*pgh*). All six major terrain classes are represented in this region: Craters, Labyrinth, Hummocky/mountainous, Plains, Dunes, and Basin and Lakes. We find that plains dominate the surface of the Soi crater region, comprising ~73% of the mapped area, followed by dunes (~14%), mountains/hummocky terrains (~12%), basin and lakes (~0.7%), labyrinth terrains (~0.5%), and crater terrains (~0.4%). We also observe empty lakes as far south as 40°N. The Soi crater region largely has the same collection and proportion of geomorphological units to other mapped regions on Titan. These results further support the hypothesis that surface processes are, broadly speaking, the same across Titan's middle and equatorial latitudes, with the exception of Xanadu.

Plain Language Summary Titan is the largest moon of Saturn and was studied by the Cassini-Huygens mission for 13 years. The mission revealed this moon to be a geologically interesting world, with Earth-like features such as lakes, dunes, rivers, and depositional plains. However, the chemistry of the moon is based on organic molecules at cryogenic temperatures, as opposed to silicate rock and water. We prepare a geomorphology map of a particular region, known as the Soi crater region, in order to classify and catalog the terrain of this region. We use data from Cassini's RADAR, Visible and Infrared Mapping Spectrometer, and Imaging Science Subsystem instruments, but map primarily with Synthetic Aperture Radar. In doing so we make interpretations about the geology of Titan's equatorial and mid-latitudes areas, which the Soi crater region encompasses. We find that broadly speaking, the Soi crater region follows trends for other equatorial and midlatitude regions of Titan, but do find a few surprises, such as mid-latitude lake features typically associated with Titan's polar regions.

1. Introduction

The Cassini-Huygens' mission revealed the once enigmatic moon Titan to be a geologically complex world, modified by both exogenic and putative endogenic processes. The largest moon of Saturn, Titan has a dense atmosphere and active hydrocarbon cycle that enables aeolian, fluvial, pluvial, and lacustrine processes. Relatively few impact craters are found (Hedgepeth et al., 2020; Neish & Lorenz, 2012; Neish et al., 2013, 2015; Werynski et al., 2019; Wood et al., 2010), confirming a geologically young surface. Organic materials, produced by long-term photochemical processing of methane and nitrogen in the upper atmosphere, cover much of Titan (Barnes et al., 2008, 2011; Brossier et al., 2018; Clark et al., 2010; Krasnopolsky, 2009; Lavvas et al., 2008;

Mackenzie et al., 2014; Soderblom et al., 2007; Solomonidou, Neish, et al., 2020; Solomonidou et al., 2018; Wilson & Atreya, 2004). Titan's equatorial zones are dominated by massive organic sand seas (Lopes et al., 2010; Lorenz, Wall, et al., 2006; Radebaugh et al., 2008; Rodriguez et al., 2014), whereas the mid-latitudes are dominated by “undifferentiated plains”: patterns of wind deposition on Titan show that, for both northern and southern hemispheres, winds transport material from both the equatorial regions and high latitudes toward the mid-latitudes (a belt at $\sim 35^\circ$), where materials are eventually concentrated and deposited as undifferentiated plains (Lopes et al., 2016; Malaska, Lopes, Hayes, et al., 2016; Solomonidou, Neish, et al., 2020). A variety of channel networks and fluvial valleys have been seen by both the Cassini orbiter and by the Huygens probe during its descent, suggesting that liquid hydrocarbons have flowed energetically across Titan's surface (Birch et al., 2016; Burr, Drummond, et al., 2013; Burr, Perron, et al., 2013; Burr et al., 2009; Langhans et al., 2012; Radebaugh et al., 2018). Some channels even still contain liquids (Poggiali et al., 2016). Lakes and seas are found at high latitudes and the poles (A. Hayes et al., 2008; Birch et al., 2016; Mitri et al., 2007; Stofan et al., 2007). Studies based on morphology have also constrained location and areal extent for polar paleoseas (e.g., Birch et al., 2018), with additional evidence for paleolakes at low latitudes (e.g., Moore & Howard, 2010). Evidence for evaporites on Titan, in particular within or around dry lakes and seas, is suggested by water-ice-poor, 5- μm bright material (e.g., Barnes et al., 2011; Michaelides et al., 2016). These evaporitic features cover 1% of the moon's surface, with the greatest areal concentration in the equatorial basins Tui Regio and Hotei Regio, and not in the poles (MacKenzie et al., 2014). Taken together, the morphology and spectral studies suggest a historically wetter Titan with a larger inventory of surface liquid hydrocarbons, with the possibility of fossil seas or lakes at low latitudes. Evidence for tectonism and possible cryovolcanism have also been identified, similarly contributing to surface modification (Jaumann et al., 2008, 2009; Lopes et al., 2007, 2013; Mitri et al., 2008, 2010; Nelson et al., 2009; Radebaugh et al., 2007; Sohl et al., 2014; Solomonidou et al., 2013, 2016; Wall et al., 2009). Mountains and hummocky materials are mostly exposed at equatorial latitudes (e.g., Radebaugh et al., 2011), but also appear in smaller areas all over the surface and are thought to be remnants of the ancient ice crust (Birch et al., 2017; Lopes et al., 2010, 2016, 2019, 2020; Malaska et al., 2020; Malaska, Lopes, Williams, et al., 2016; Schoenfeld et al., 2021; Williams et al., 2011).

Planetary geologic mapping is a tool that helps us inventory and interpret the regional or global geologic history of planets and moons. For Saturn's moon Titan, we inventory the landscape using geomorphological terrain units defined by common radar backscatter and morphological characteristics (e.g., Lopes et al., 2016, 2020; Malaska, Lopes, Williams, et al., 2016; Schoenfeld et al., 2021), which may or may not correspond to true geological units (which are defined by rock composition, age, and history). We therefore refer to the map presented in this study as a geomorphologic map, which nonetheless allows us to infer geologic relationships. As such, the goal of this endeavor is to reconstruct the geologic history of the Soi crater region, which is representative of the transition between the equatorial, mid-latitude, and high latitude northern regions of Titan, through detailed geomorphological mapping.

Our completed map details the types and extents of geomorphologic units present in the Soi crater region. We use the map to infer relative stratigraphy between units and the possible geological processes responsible for their formation and evolution. The mapping presented here follows the general principles of previous Titan mapping (e.g., Stofan et al., 2006) and is a continuation of the detailed geomorphological mapping effort presented in Malaska, Lopes, Williams, et al. (2016) and Schoenfeld et al. (2021). For this paper, we are particularly interested in examining the transition between the equatorial and mid-latitude terrains (such as mapped by Lopes et al. (2010), Malaska, Lopes, Williams, et al. (2016), and Schoenfeld et al. (2021)) and the high latitude regions mapped by Birch et al. (2017). We used the Cassini's Synthetic Aperture Radar (SAR) data as the basemap, but we also incorporated information from non-SAR data sets, including microwave emissivity, topography, visible and infrared reflectance. A better understanding of such geologic processes will aid in the science return of Dragonfly, where new, high-resolution data can be used to test terrain evolution models derived from the detail mapping, and additionally guide the science objectives for future missions (e.g., Lorenz et al., 2021; Rodriguez et al., 2022; Sulaiman et al., 2021; Tobie et al., 2014).

2. Location and Geologic Setting

Our mapping encompasses the Soi crater region (Figure 1), which we define as the area spanning from longitude 110° to 180°W (from right to left, covering 70° longitudinally; see green square in Figure S1; all tables, figures, and additional text in Supporting Information S1 will be symbolized by “S”) and from latitude 0° to 60°N . A

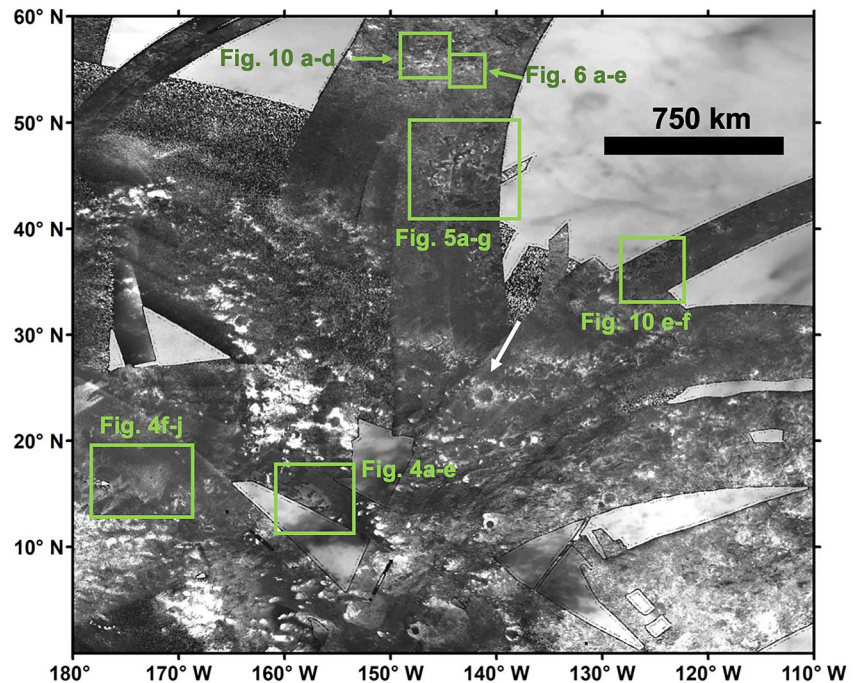


Figure 1. Synthetic Aperture Radar map of the Soi crater region. Locations of figure subsets included in this paper indicated with green boxes. The white arrow points to the Soi crater. The total area of the Soi crater region is $8 \times 10^6 \text{ km}^2$. Scale bar applies to equatorial latitudes. North is at the top.

portion of this area, from 170° to 180°W , was previously examined in Malaska, Lopes, Williams, et al. (2016) as part of the Afekan crater region map (yellow square in Figure S1 in Supporting Information S1). However, for our mapping purposes going forward we define Afekan as the area spanning the region from longitude 110°E to 180°W and from latitude 0° to 60°N . We expanded the Soi crater region to 180°W in order to include western features in our analysis. Figure 1 shows the Soi crater regional map with location of subsequent figures within this paper indicated in green. Figure S1 in Supporting Information S1 shows a context map of where the region is located as well as the overlap area previously published in Malaska, Lopes, Williams, et al. (2016) and the South Belet region (magenta square in Figure S1 in Supporting Information S1) published by Schoenfeld et al. (2021).

The area contained in this region amounts to $\sim 8 \times 10^6 \text{ km}^2$ ($\sim 10\%$ of Titan's surface). However, detailed mapping was only done for the areas within the Soi crater region covered at high resolution by SAR ($4.7 \times 10^6 \text{ km}^2$) and therefore, the fraction of Titan's total surface that was mapped at high-resolution is $\sim 5.6\%$. The rest of the area was covered by non-SAR data (emissivity, Imaging Science Subsystem [ISS], and Visible and Infrared Mapping Spectrometer [VIMS]), and mapped at lower resolution (see Section 3.1.2). The Soi crater region contains a wide variety of terrain units and, when compared to the Afekan (Malaska, Lopes, Williams, et al., 2016) and South Belet regions (Schoenfeld et al., 2021), appears to be representative of Titan's mid-latitudes and equator. The region contains the NE section of Shangri-La dune field, a vast field of equatorial dunes at lower latitudes, 10 impact craters we identify with confidence (including Soi), a large number of empty lakes, part of the Xanadu region, and large expanses of plains at mid-latitudes.

3. Geomorphological Mapping

To extract morphological information, Titan's hazy atmosphere limits the usefulness of visible and infrared data, as it scatters light at these wavelengths. RADAR is therefore the primary Cassini instrument used for studying Titan's geology since the longer wavelengths of microwave radiation interacts with the surface with negligible atmospheric interference. We recognize that, from SAR images alone, the interpretation can be limited (e.g., Bratsolis et al., 2012). We therefore used SAR as the base data set, from which we drew the contacts between units, but also used data from other modes of the RADAR instrument (altimetry, SARTopo, and radiometry) and data from VIMS and ISS to provide additional constraints on the terrain assignment.

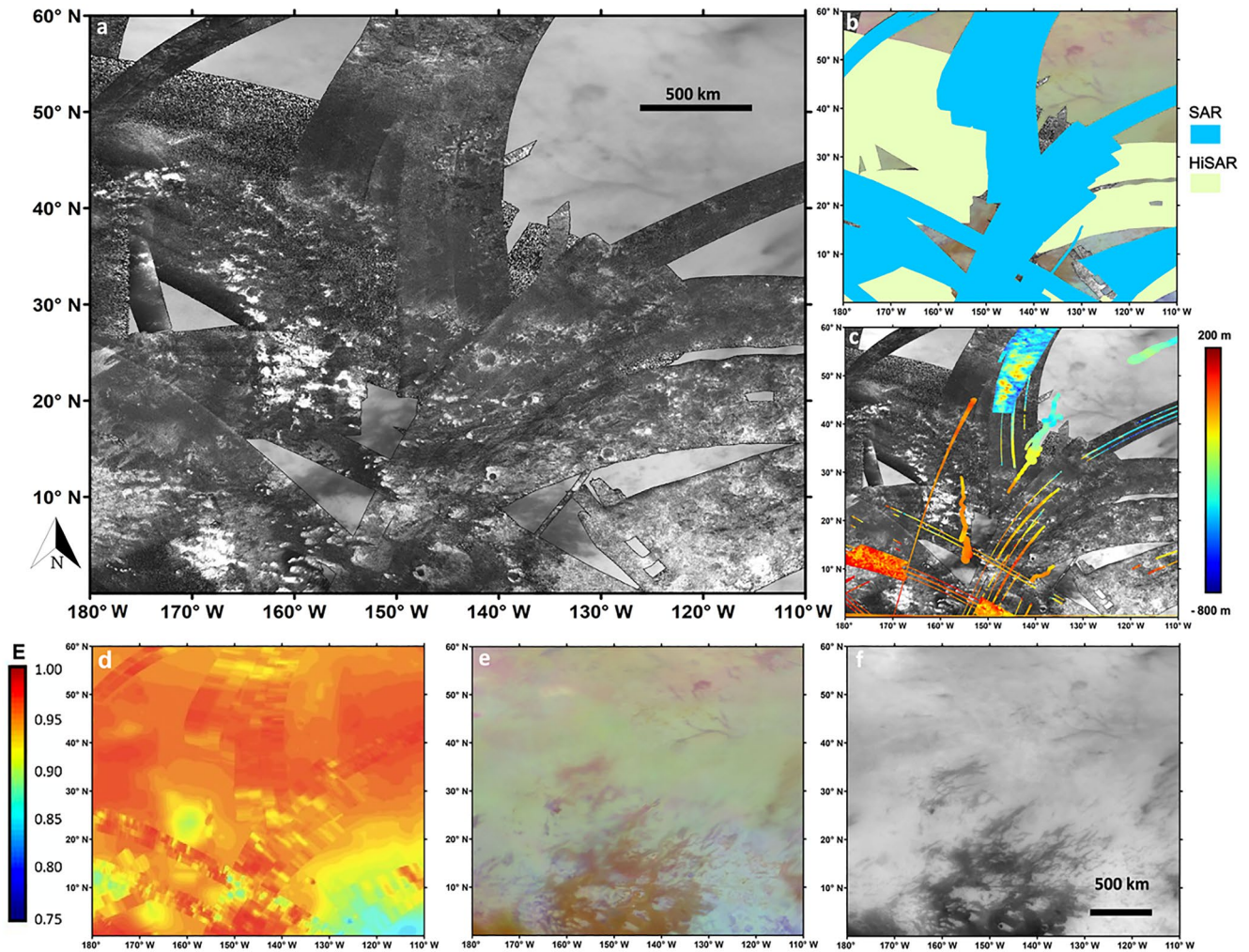


Figure 2. Different types of Cassini data covering the Soi crater region. (a) Synthetic Aperture Radar (SAR), (b) SAR and high-altitude SAR (HiSAR), (c) SARTopo and Digital Terrain Model, (d) emissivity, (e) Visible and Infrared Mapping Spectrometer, and (f) Imaging Science Subsystem.

3.1. Data Sets

3.1.1. SAR

Cassini's RADAR is a multimode Ku-band (13.78 GHz, $\lambda = 2.17$ cm) instrument (Elachi et al., 2005, 2006; Stiles, 2017a, 2017b) that operates in four modes: SAR, altimetry, scatterometry, and radiometry. We used data from the RADAR in its SAR mode to perform our initial geomorphological mapping and define the boundaries of the terrain contacts (Figures 2a and 2b). Radar data is incidence angle corrected to be the same globally and for all terrains (Stiles et al., 2006); relative backscatter is then used to evaluate terrain brightness. Some terrain types are more sensitive to incidence angle than others (e.g., Malaska, Lopes, Williams, et al., 2016), so a uniformly applied incidence angle correction introduces some uncertainty in our mapping, although we use overlapping SAR swaths (when available) to mitigate this uncertainty. Radar backscatter returned from the surface depends on roughness, incidence angle of the beam, dielectric constant of the material, slope angle orthogonal to the beam, volume scattering, structural properties, and subsurface inhomogeneities (such as layers of varying dielectric constant). A change of any one of these properties can produce a different radar backscatter; for example, a rough surface and a smooth surface of the same composition could present different properties to radar, and terrains of different compositions, but similar backscatter functions, could be undistinguishable in SAR images. Details on the SAR and high-altitude SAR (HiSAR) nature of the data can be found in Section S1 and Table S1 in Supporting Information S1.

3.1.2. Non-SAR

We also used data from the RADAR's radiometry mode and altimeter, in addition to VIMS and ISS observations (Section S1 in Supporting Information S1). Figure 2 shows the different types of data used for the geomorphological mapping:

- a. SAR swaths were used as a basemap for geomorphological mapping. Underlying the SAR mosaic is the globally-controlled ISS mosaic, from Karkoschka et al. (2017, LPSC). Atmospheric scattering limits the usefulness of this mosaic. Soi crater is located near the center of the image (24.3°N, −140.9°W) and a portion of Xanadu is seen on the lower right.
- b. SAR and HiSAR coverage, where light green indicates the HiSAR swaths and blue indicates the high-resolution SAR swaths, as listed in Table S1 in Supporting Information S1. Small parts of HiSAR that are not colored green in the figure were not used in our mapping due to significant noise. The background is VIMS RGB color ratio mosaic that complements the SAR swaths to cover the entire Soi crater region (description in Le Mouélic et al. (2019) and Seignovert et al. (2019)), and has been manually georeferenced to the SAR base mosaic. The RGB composite is 1.59/1.27 μm (R), 2.03/1.27 μm (G), and 1.27/1.08 μm (B).
- c. Elevation data. SARTopo data were obtained by the method described in Stiles et al. (2009). For SARTopo (along the SAR swath), colors represent relative elevations within each swath. Cooler colors are lower (to −800 m), and warmer tones are higher (to +200 m) relative to the nominal 2,575 km radius sphere. Because of relatively large errors involved in SARTopo when compared across swaths, we only use the relative elevations along an individual swath track to help mapping; they do not provide an absolute scale. Digital Terrain Models (DTMs) are also available with a typical error of ~ 100 m (Corlies et al., 2017; Kirk et al., 2012). Altimetry data are consistent across passes as shown by the overlap in the lower left of the region.
- d. Emissivity map from Janssen et al. (2016). Comparison with panel (a) shows that Xanadu has relatively low emissivity (cold colors), while the undifferentiated plains and dunes have higher (warm colors) emissivity.
- e. VIMS mosaic of the region prepared from a global VIMS mosaic (same details as for (b)).
- f. The ISS mosaic without the overlaid SAR mosaic.

More information on these instruments and their data can be found in Section S1 in Supporting Information S1.

3.2. Mapping Area and Technique

In general, we follow the technique outlined in Malaska, Lopes, Williams, et al. (2016), Malaska et al. (2020), Lopes et al. (2020), and Schoenfeld et al. (2021), and use SAR swaths as our primary basemap for conducting our geomorphological mapping. However, in this study we describe in greater detail the technique we developed for mapping beyond the boundaries of the SAR, that is, non-SAR mapping, that makes use of lower resolution data sets such as ISS, VIMS, radiometry, and HiSAR in order to provide a more complete picture of Titan's surface characteristics (Lopes et al., 2020).

3.2.1. SAR Mapping

The SAR swaths were mosaicked and loaded into the ArcGIS™ 10.6 (ESRI) software package and then used to categorize the surface based on morphological and backscatter properties. Contacts between terrains of different radar backscatter or morphological signatures were drawn, the boundaries being determined by following procedures described in previous studies (e.g., Birch et al., 2017; Lopes et al., 2010, 2016; Malaska, Lopes, Williams, et al., 2016; Schoenfeld et al., 2021; Stofan et al., 2007; Williams et al., 2011). We defined gradational contacts between units if a clear delineation could not be made at the resolution of the SAR images (~ 1 km). Using the drawn contacts, we built polygons and assigned a terrain unit classification based on feature morphology and radar backscatter. Data from SARTopo, radiometry, ISS, and VIMS, while not used to delineate units in the high-resolution contact mapping, were used to refine terrain classification as outlined in Malaska, Lopes, Williams, et al. (2016).

In general, we only use the higher-resolution SAR swaths for mapping at an image scale of 1:800,000 (Greeley & Batson, 1990). However, in certain areas, HiSAR (a high-altitude SAR imaging mode with multi-km scale resolution) of sufficient quality were included in the base map mosaic and used for mapping. We determined if a HiSAR swath was of suitable quality based on the capacity to distinguish terrain units and subunits with the same level of detail as with a regular SAR swath; for example, if we were able to distinguish between “degraded

hummocky terrains,” “hummocky,” and “mountainous.” In total ~32% of the Soi crater region was mapped using the high-resolution SAR, while ~26% of the mapped area was done so with “good” HiSAR. Some data (particularly HiSAR with degraded resolution) were considered not to be of sufficient quality to map at the scale of 1:800,000, though these could potentially be mapped at larger scales (see Section 3.2.2).

3.2.2. Non-SAR Mapping

The mapping procedure outlined in Malaska, Lopes, Williams, et al. (2016), Lopes et al. (2020), and Schoenfeld et al. (2021) involves correlating the SAR mapping units with characteristic signal return in radiometry, VIMS, and ISS. For example, the “featureless sand sheets” appear dark in radar, but they also appear dark in ISS, brown-purple in RGB VIMS false colors (1.59/1.27 μm (R), 2.03/1.27 μm (G), and 1.27/1.08 μm (B)), and have high emissivity in radiometry. This combination of characteristics is part of the definition established for the “featureless sand sheets” unit. Similarly, undifferentiated plains appear bland and dark in SAR and HiSAR but appear bright in ISS and have high emissivity in radiometry. We leveraged previously established correlations and used them to extend the mapping to the areas not imaged by SAR or HiSAR. The non-SAR areas were mapped at a much lower resolution than the SAR area, at a scale of 1:20,000,000 (Lopes et al., 2020), and make up ~42% of the mapped region. We identify this larger scale mapping by labeling contacts drawn using the ISS, VIMS, as “approximate”.

Finally, for areas where HiSAR exists but is of insufficient quality, that is, unable to distinguish between “degraded hummocky terrains,” “hummocky,” “mountainous,” etc., we still rely primarily on the radar backscatter for unit delineation, but use the NonSAR units for terrain assignment. For example, a unit that is both radar dark in the HiSAR and elongated in the E-W direction we assign as “undivided dunes,” whereas a radar bright unit with globular morphology we assign as “undivided hummocky/mountainous.” Contacts are drawn as “inferred” for the low-resolution HiSAR.

4. Geomorphologic Mapping Results

4.1. SAR Units

The terrain classes and units, including the three new mapping units, in the Soi crater region were initially identified using the SAR mosaic basemap. The main terrain classes are Craters, Hummocky/mountainous, Labyrinth, Plains, dunes, and Lake and Basin. Each main terrain class is subdivided into terrain units based on morphology (general shape, texture, and basic appearance) and radar backscatter. In general, the radar backscatter is broadly classified as “high,” “medium,” “low,” or “variable” for each of the units. The main terrain units are described in Table 1 and local examples of each unit are shown in Figure 3. The terrain unit abbreviations are a concatenation where the first letter refers to the broad terrain class (e.g., *p* for plains), the second letter stands for a finer descriptor for the terrain type (e.g., *u* for undifferentiated), and the last letter indicates the relative radar backscatter compared to the other units (e.g., *l* for low). Therefore, the undifferentiated plains abbreviation “*pul*,” refers to “plains-undifferentiated-low,” indicating a plains unit with no distinct features and with a radar backscatter that is relatively lower (darker) than other units on Titan. For detailed description of the units, see Malaska, Lopes, Williams, et al. (2016) (Section 4), Lopes et al. (2020) (Methods), and Schoenfeld et al. (2021) (Section 4). As with the Afekan and South Belet maps, we additionally include physical features (such as channels, impact features, and putative cryovolcanic features (Lopes et al., 2013) as a polyline or additional shape layer on the geomorphological map. However, the Soi crater region does not contain any putative cryovolcanic feature. See Section 4.3 for the resulting geomorphology map and Section 5.1.2 for the physical feature map.

In this study, we describe in detail three new mapping units not previously discussed in our mapping investigations: the bright gradational plains (*pgl*), the sharp-edged depressions (SEDs) (*bse*), and the ramparts (*brh*). It should be noted, that the SEDs and the ramparts are features that have been identified and described for Titan, and are “new” only in the context of our mapping schema, but not new in the literature (e.g., Birch et al., 2017, 2019; Solomonidou, Le Gall, et al., 2020). Similarly, bright gradational plains (*pgl*) are consisted with features discussed in existing literature, but were not labeled as such (e.g., Radebaugh et al., 2018). We describe the characteristics of the units below as well as offer interpretations. Table 1 summarizes all the identified terrain classes, units, and unit codes in addition to locations of characteristic examples of the units.

Table 1
Terrain Class, Terrain Units, Terrain Unit Code, and Type Feature Locations

Data set	Terrain class	Terrain unit name/code/description	Location (example)	Data set properties	Relative topography
SAR	Plains	Undifferentiated plains (<i>pu</i>): most extensive unit on Titan, dominate mid-latitudes, bland appearance in radar. Interpreted as wind-blown deposits of organic materials	33.8°N, 145.7°W	SB: medium-bright R: 0.96–0.97	Lower than craters/ mountains
		Variable plains (<i>pfv</i>): regions containing broad patches of SAR dark and bright materials. Interpreted as deposits of organics mixed with eroded material derived from mountains and hummocks	10.2°N, 119.1°W	SB: variable R: 0.91–0.96	Variable
		Scalloped plains (<i>psv</i>): radar low to radar medium patches mostly at high latitudes, lobate morphology, and patchy internal texture. Interpreted as eroded crustal material partially covered by organics, or potentially remnant evaporitic material	58.7°N, 141.7°W	SB: medium-dark R: 0.93–0.94	Variable
		Dark irregular plains (<i>pil</i>): irregular patches of SAR-dark terrains with lobate boundaries. Interpreted as low-lying basins dampened by liquids	36.7°N, 125.4°W	SB: medium-dark R: 0.97–0.98	Locally low
		Streak-like plains (<i>psl</i>): radar bright with diffuse-internal texture and elongated morphology, generally parallel to local dunes. Interpreted as aeolian deposits of radar bright materials	30.4°N, 147.3°W	SB: bright R: 0.94–0.96	Not discernible
		Bright gradational plains (<i>pgh</i>): radar bright with diffuse but fairly uniform internal texture and gradational boundaries. Interpreted as radar bright material deposited by fluvial action	14.5°N, 157.9°W	SB: medium-bright R: 0.92–0.93	Locally low
		Radio/ISS/VIMS		Undivided plains (<i>pu</i>): broad plains unit that may contain undifferentiated plains, scalloped plains, lineated plains, and variable featured plains	49.5°N, 167.2°W
Undivided dark plains (<i>pdu</i>): broad plains unit that may contain dark irregular plains, streak-like plains, and perhaps a certain amount of labyrinth terrains	45.6°N, 116.9°W			VR, IB: gray R: 0.94–0.98	Variable
SAR	Dunes	Featureless sand sheets (<i>ds</i>): featureless SAR-dark areas that may be elongated in the W-E direction. Interpreted as organic sand deposits deposited by aeolian action	16.9°N, 158.5°W	SB: dark R: 0.93–0.96	Variable
		Linear dunes (<i>dl</i>): parallel to sub-parallel SAR-dark lines on a variable backscatter substrate. Interpreted as organic longitudinal dunes	4.5°N, 156.3°W	SB: dark R: 0.96–0.98	Elevated with rises and falls
Radio/ISS/VIMS		Undivided dunes (<i>du</i>): broad dune unit that may contain linear dunes, featureless sand sheets, and reticulated dunes. Only found within the equatorial regions	7.8°N, 134.2°W	HSB: dark R: 0.93–0.97 IB: dark VR: brown	Variable

Table 1
Continued

Data set	Terrain class	Terrain unit name/code/description	Location (example)	Data set properties	Relative topography
SAR	Mountains/ Hummocky/ Labyrinth	Mountain (<i>hm</i>): elongated to globular features with evident SAR bright/dark pairing. Interpreted as rugged exposures of ancient crust	10.6°N, 173.7°W	SB: bright R: 0.89–0.90	Elevated
		Hummocky (<i>hh</i>): radar bright globular regions generally small in areal extent. Interpreted as highland exposures of ancient crust	8.8°N, 149.2°W	SB: bright R: 0.85–0.90	Elevated
		Degraded hummocky (<i>hdm</i>): radar high to radar medium exposures of hummocky-like materials. Interpreted as remnant hummocks that have been partially buried by organics or eroded	24.5°N, 134.3°W	SB: bright R: 0.93–0.94	Locally raised
		Pitted hummocky (<i>hph</i>): radar-bright hummocks populated by radar-dark, pit-like structures. Interpreted as fine grained, low backscatter materials deposited in pre-existing depressions in the exposed icy crust	8.2°N, 115.2°W	SB: bright R: 0.86–0.90	Elevated
		Finely dissected labyrinth (<i>lbf</i>): large regions of relatively featureless, high-standing plateaux. Any internal texture consists of thin, high radar-backscatter patterns. Interpreted as labyrinth with tightly spaced subparallel or orthogonal channels/valleys that are just below the resolution limit (definition from Malaska et al. (2020))	48.6°N, 147.3°W	SB: mid-gray R: 0.94–0.97	Elevated
Radio/ISS		Undivided mountain chains/hummocky areas (<i>hu</i>): broad hummocky unit that may contain hummocky terrains, mountains, degraded hummocky, and pitted hummocky terrains.	4.0°N, 168.1°W	SB: mid-gray R: 0.84–0.90	Locally high
SAR	Craters	Crater rim (<i>crh</i>): high backscatter circular exposure. Interpreted as a remnant impact crater rim	25.9°N, 200.3°W	SB: bright R: 0.93–0.94	Locally raised
		Crater ejecta (<i>ceh</i>): radar bright materials grading radially out from crater rim. Interpreted as impact ejecta	24.3°N, 141°W	SB: bright R: 0.93–0.94	Locally raised
		Crater fill 3 (<i>cf3</i>): featureless, radar dark materials completely or partially enclosed by a rim. Interpreted as either material eroded from the rim or organic wind-blown deposits	24.3°N, 141°W	SB: dark R: 0.93	Lower than rim
SAR	Lakes	Sharp-edged depression (<i>bse</i>): depressions with radar-medium floors and lobate boundaries defined by a sharp, radar-bright boundary. Interpreted as an empty lake basin	55.4°N, 141.3°W	SB: medium R: 0.92–0.94	Low
		Ramparts (<i>brh</i>): SAR-bright mound-like annuli extending away from the lake for up to tens of kilometers from the shoreline	54.7°N, 144°W	SB: bright R: 0.92–0.94	Locally raised

Note. Data set properties: SAR backscatter (SB), HiSAR backscatter (HSB), VIMS RGB (VR), ISS brightness (IB), Radiometry (R). We use undifferentiated plains as the reference standard for our qualitative descriptions, that is, dune units are radar “dark” with respect to the undifferentiated plains, which are radar “medium-bright”.

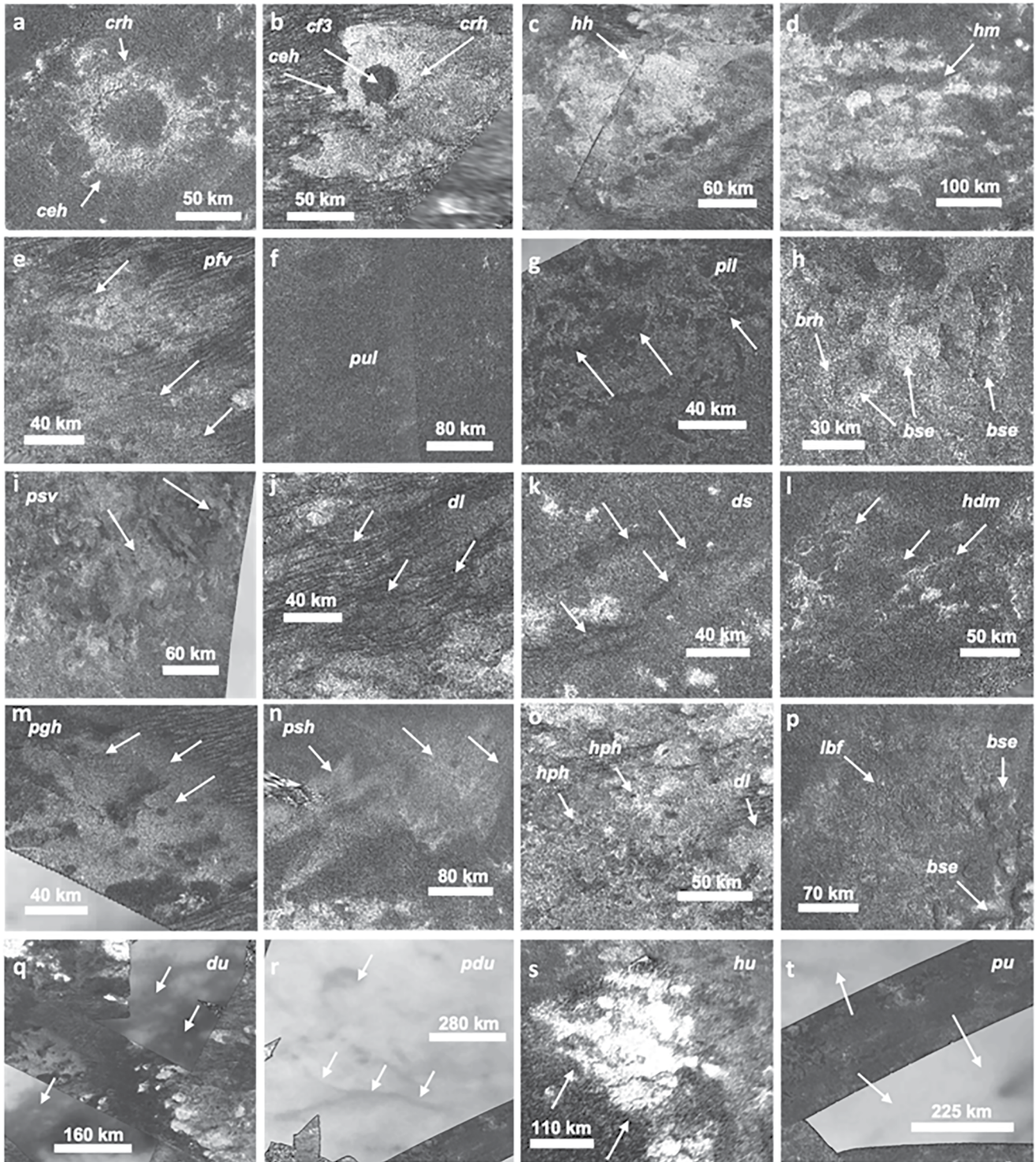


Figure 3. Synthetic Aperture Radar images of type examples of terrain units used within the Soi crater region. White arrows point to the type feature. The code references the terrain code in the text and in Table 2. Abbreviation key: (a) (image center: 24.3.5°N, 141°W) *crh* = crater rim, *ceh* = crater ejecta, (b) (11.5°N, 141°W) *cf3* = crater fill 3, (c) (7.9°N, 149.8°W) *hh* = hummocky, (d) (9.8°N, 174.5°W) *hm* = mountains, (e) (7.8°N, 163.7°W) *pfv* = variable-featured plains, (f) (34.3°N, 144.3°W) *pul* = undifferentiated plains, (g) (36.8°N, 124.9°W) *pil* = dark irregular plains, (h) (55.3°N, 142.5°W) *bse* = sharp-edged depressions, *brh* = rampart (i) (57.6°N, 142°W) *psv* = scalloped plains, (j) (16.8°N, 137.4°W) *dl* = dark linear dunes, (k) (20.7°N, 142.9°W) *ds* = featureless sand sheets, (l) (27.7°N, 128.4°W) *hdm* = degraded hummocky, (m) (14.7°N, 157.4°W) *pgh* = bright gradational plains, (n) (15.4°N, 174.4°W) *psh* = streak-like plain, (o) (8.9°N, 115.3°W) *hph* = pitted hummocky, (p) (11.5°N, 141°W) *lbf* = finely dissected labyrinth, (q) (15.7°N, 153.3°W) *du* = undivided dunes, (r) (45.6°N, 126.6°W) *pdu* = undivided dark plains, (s) (4°N, 168.1°W) *hu* = undivided hummocky/mountainous, and (t) (38.3°N, 120°W) *pu* = undivided plains.

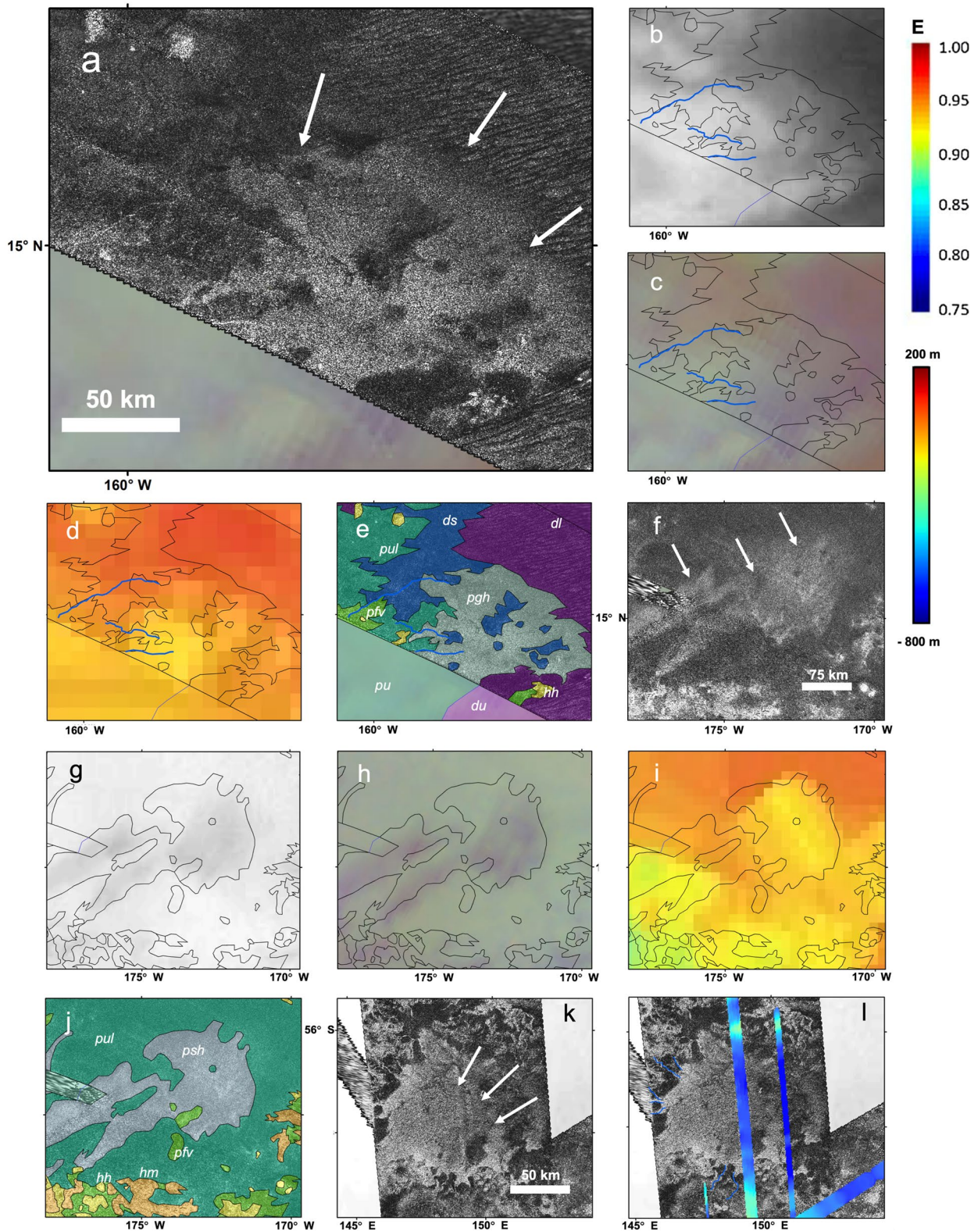


Figure 4.

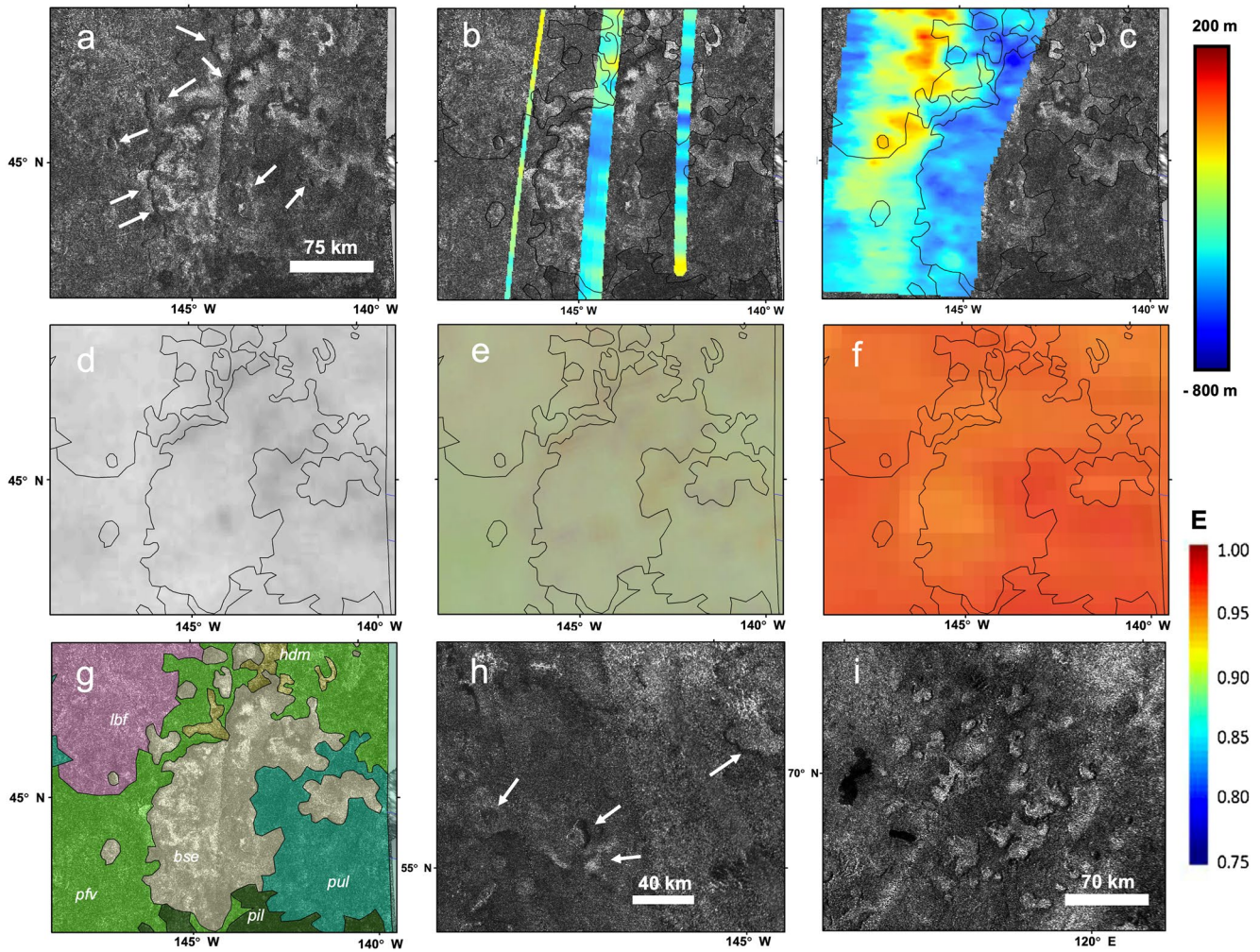


Figure 5. Examples of sharp-edged depressions (*bse*) in the mid-latitudes of the Soi crater region: (a) Synthetic Aperture Radar (SAR) mosaic, several of the empty depressions indicated by white arrows. Look direction is to the right. (b) SARTopo overlay on the SAR mosaic with contacts between mapped terrain units. (c) Digital Terrain Model (DTM) overlay on the SAR mosaic. (d) Imaging Science Subsystem mosaic with terrain contacts. (e) Visible and Infrared Mapping Spectrometer RGB mosaic with terrain contacts (RGB colors controlled by 2, 1.59, and 1.27 μm channels respectively). (f) Emissivity map with terrain contacts. (g) Annotated terrain unit mapping on the SAR mosaic. Yellowish brown: degraded hummocky terrains (*hdm*); beige: sharp-edged depressions (*bse*); dark pink: finely dissected labyrinth (*lbf*); dark green: dark irregular plains (*pil*); lime green: variable featured plains (*pfv*); turquoise green: undifferentiated plains (*pul*). (h) Several instances of sharp-edged depressions (SEDs) identified in the Afekan crater region. (i) SAR image of an area in the north pole with empty and filled SEDs.

4.1.1. Bright Gradational Plains (*pgh*)

The bright gradational plains (*pgh*) (type area: 14.5°N, 157.9°W) appear bright in radar, with a fairly uniform interior texture but with diffuse or gradational boundaries (Figure 4a). Channels can be seen within or adjacent to the unit (Figures 4b–4e). Microwave emissivity of this unit (Figure 4d) is relatively low (~ 0.92), appearing lower than the undifferentiated plains (*pul*) (~ 0.97), but not quite as low as the bright alluvial plains (*pah*), a unit present

Figure 4. Example of bright gradational plains (*pgh*) (a–e) and streak-like plains (*psh*) (f–j) within the Soi crater region: (a and f) Synthetic Aperture Radar (SAR) mosaic of the *pgh* and *psh* indicated by white arrows respectively. (b and g) Imaging Science Subsystem mosaic of the *pgh* and *psh* overlain with terrain unit contacts. Blue lines indicate channels identified in the image. (c and h) Visible and Infrared Mapping Spectrometer RGB mosaic of the *pgh* and *psh* with contacts (RGB colors controlled by 2, 1.59, and 1.27 μm channels respectively). (d and i) Emissivity map overlain with contacts. (e and j) Annotated terrain unit mapping on the SAR mosaics. Magenta corresponds to linear dunes (*dl*); blue to featureless sand sheets (*ds*), purple to undivided dunes (*du*); yellow to hummocky terrains (*hh*); dark yellow to mountains (*hm*); turquoise green to undifferentiated plains (*pul*); lime green to variable plains (*pfv*); gray to gradational plains (*pgh*); blue gray to streak-like plains (*psh*); and mint green to undivided plains (*pu*). The blue lines in panels (b–e) correspond to channels. (k) SAR mosaic of a “SAR-bright basin” as discussed in Radebaugh et al. (2018), located in South Ching Tu. Visible in the image are triangular, SAR-bright fans that grade away into moderately SAR-bright materials consistent with our definition of “bright gradational plains” (indicated by white arrows). (l) The same feature but with topographic information and channels indicated with blue lines. The *pgh* examples in the Soi crater region do not have topo traces overlapping the feature in such a way.

in the South Belet region (Schoenfeld et al., 2021). Similarly, in VIMS the unit appears blue in RGB (Figure 4c) but not quite to the same degree as the bright alluvial plains (Schoenfeld et al., 2021), which seem to be associated with channels (e.g., Barnes et al., 2007; Langhans et al., 2012). In ISS the unit appears variable (Figure 4b), characterized as varying patches of medium dark and bright. We also compare the bright gradational plains to the bright streak-like plains (*psh*). Figure 4 present examples of both *pgh* and *psh* from the Soi crater region as shown in SAR and their equivalent annotated map (Figures 4e and 4j and 4e), as well as their compared appearance in VIMS, ISS, and SARTopo. Both units have similar signatures in radar (Figures 4a and 4f), emissivity (Figures 4d and 4i), VIMS (Figures 4c and 4h), and ISS (Figures 4b and 4g), yet have different morphological boundaries. Their similarities suggest a shared origin with divergent endmember processing that accounts for their differences in morphology. We discuss further the similarity of these units in Section 5.1.3.2 and offer a more detailed geologic interpretation.

Due to their lower microwave emissivity compared to the other plains units (Figure 4d), such as the *pul* or *pfv*, and due to their association with adjacent channels (blue lines in Figure 4) and highlands, we interpret the bright gradational plains as high backscatter material originating from fluvial processes. Their blue appearance in VIMS RGB colors (Figure 4c), indicates spectral characteristics that may be consistent with that of water-ice (e.g., Barnes et al., 2007; Coutelier et al., 2021; Langhans et al., 2012). Both *pgh* and *psh* terrain units appear similar in VIMS and ISS to the linear (*dl*) and undivided (*du*) dunes terrain units. Morphologically, the bright gradational plains are broader than the bright alluvial plains and lack their planform triangular morphology. We specifically interpret the *pgh* units as broad plains of SAR bright materials originating from alluvial fans and channels, perhaps accumulating in lowlands, similar to the SAR-bright lowlands described in Radebaugh et al. (2018) (Figures 4k and 4l), eventually interacting or transitioning into darker plains/dunes. The *pgh* similarly may contain coalescing alluvial fans and channels that are unable to be individually resolved in the SAR. The broad reach of the bright gradational plains may also explain why they do not appear as radar-bright as the bright alluvial plains: further away from the highlands, the abundance of SAR-dark materials increases, consistent with the presence of finer grained materials capable of being transported over larger distances, and/or indicating the intrusion and mixing of organics sands from adjacent dunes or plains. The medium emissivity of the bright gradational plains supports this narrative, suggesting that loose conglomerates of fluvial materials, which favor volume scattering, have since been mixed or buried by smoother, smaller-grained materials, dampening scattering effects.

4.1.2. Sharp-Edged Depressions (*bse*)

The SEDs (type area: 55.4°N, 141.3°W) are quasi-circular depressions that are either fully or partially enclosed by narrow rims (<10 km wide) that are several hundreds of meters higher than the surrounding area (Birch et al., 2019). The depressions have steep sloping walls that descend rapidly to relatively flat floors (e.g., A. G. Hayes et al., 2017) that span the entire interior of these depressions, which appear radar medium to radar dark with uniform internal texture. The depressions are often entirely closed, with no evidence for inflow or outflow morphology (A. G. Hayes et al., 2017). Many SEDs have a bright-dark pairing around their boundary that correlates to elevated rim features on the order of hundreds of meters (A. G. Hayes et al., 2018; Birch et al., 2019). This pattern is similar to quasi-specular increases in backscatter seen on Titan's dunes and occurs due to slopes oriented perpendicular to the radar (Birch et al., 2019).

We interpret several features in the Soi crater region as SEDs with terrain unit code “*bse*” (Figure 5). The SEDs of the Soi crater region are (Figure 5a) morphologically consistent with the SEDs described in A. G. Hayes et al. (2017), and Birch et al. (2017, 2019) (Figure 5i). The morphological similarities between filled and empty SEDs (e.g., A. Hayes et al., 2008, A. G. Hayes et al., 2017; Birch et al., 2019), and the non-existence of radar-dark return characteristic of liquids, suggest that the dry SEDs represent previously filled, but now empty, lakes (Figure 5i). Hence, we interpret the *bse* unit as a now empty lake basin, representing an increased latitudinal extent of lacustrine processes previously though of as restricted to the polar regions. Figure 5g shows a parts of the annotated map of the Soi crater region including the *bse*.

4.1.3. Ramparts (*brh*)

Ramparts (*brh*) (type area: 54.8°N, 144°W) are SAR-bright mound-like annuli that encircle a small population of Titan's lakes (Figure 6a). They extend up to 10s of kilometers away from the shore of certain lakes (Solomonidou, Le Gall, et al., 2020) and appear locally elevated with respect to the surrounding terrain (Figures 6b and 6c).

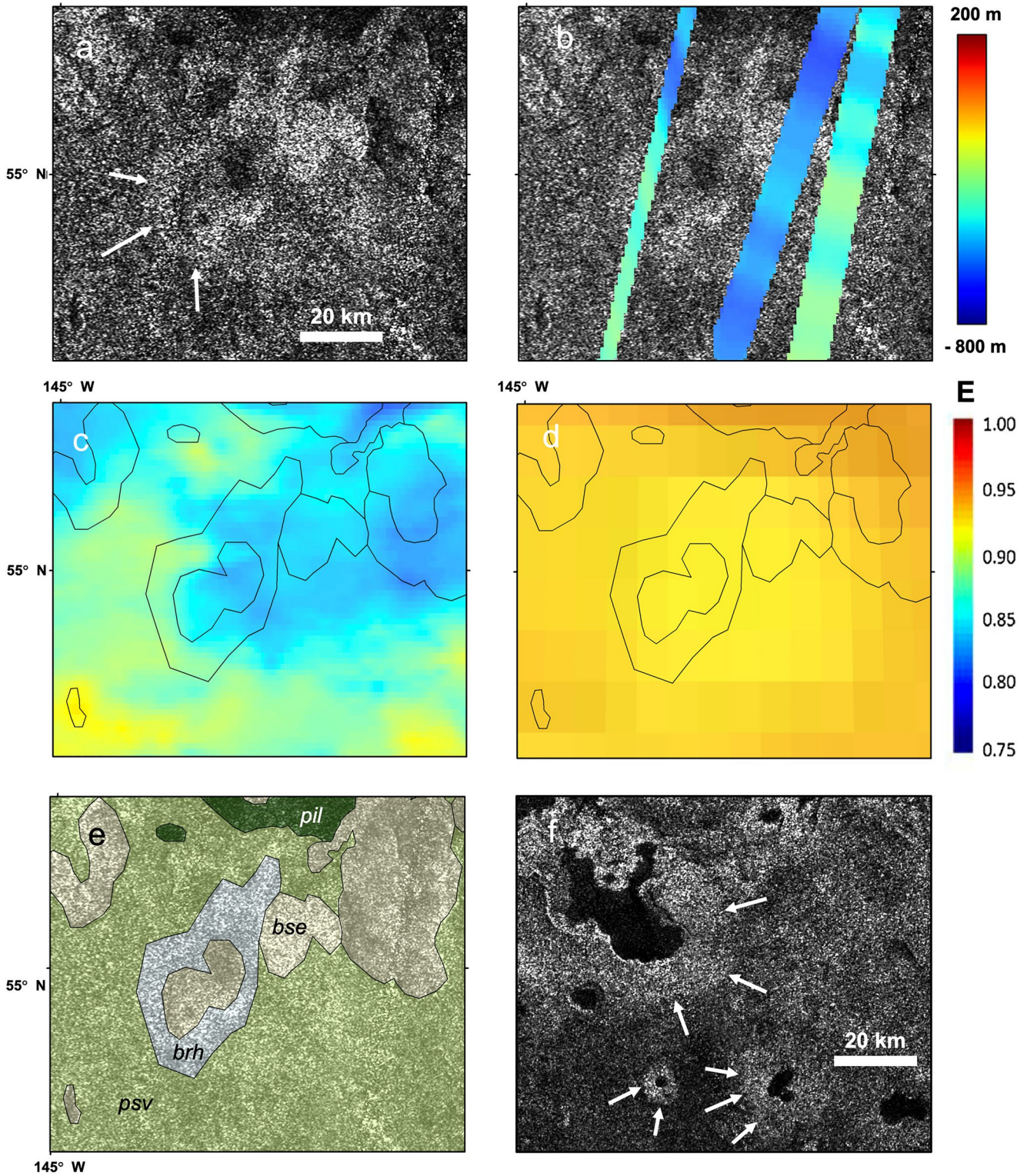


Figure 6. Examples of ramparts (*brh*) in the mid-latitudes of the Soi crater region: (a) Synthetic Aperture Radar (SAR) mosaic, a rampart around one of the empty depressions indicated by white arrows. Look direction is to the right. (b) SARTopo overlain on the SAR mosaic. (c) Digital Terrain Model overlain on the SAR mosaic with contacts between mapped terrain units. (d) Emissivity map with terrain contacts. (e) Annotated terrain unit mapping on the SAR mosaic. Beige: sharp-edged depressions (*bse*); dark green: dark irregular plains (*pil*); olive green: scalloped plains (*psv*); light blue-gray: ramparts (*brh*). (f) SAR image of an area in the north pole with ramparts that were analyzed in Solomonidou, Le Gall, et al. (2020).

SAR-bright, raised ramparts were first described in Solomonidou, Le Gall, et al. (2020), having been identified around some of the north polar lakes. The ramparts of the Soi crater region are morphologically consistent with the ramparts described in Solomonidou, Le Gall, et al. (2020), and thus we consider them the same feature (Figure 6f). Emissivity analysis of the raised ramparts show them to be radiometrically warm, close in value to that of Titan's labyrinth terrains and to the empty lake floors, pointing to an organic-rich composition (Figure 6d). This compositional similarity is confirmed by VIMS analysis that shows that the infrared spectral response of the raised ramparts is similar to that of many of the empty lake floors, suggesting that both features are covered or made up of comparable materials (Solomonidou, Le Gall, et al., 2020).

4.2. Non-SAR Units

We use non-SAR data in an effort to maximize the use of Cassini surface data and to provide the most complete geomorphological map for the Soi crater region. These “non-SAR” mapping units have not been described in our previous mapping studies (e.g., Malaska, Lopes, Williams, et al., 2016; Schoenfeld et al., 2021), but were briefly mentioned in Lopes et al. (2020). We thus elaborate on the descriptions and associated interpretations for the non-SAR mapping units that appear in the Soi crater region, which include undivided dunes (*du*), undivided hummocky/mountainous (*hu*), undivided dark plains (*pdu*), and undivided plains (*pu*).

4.2.1. Undivided Dunes (*du*)

The undivided dunes (*du*) (type area: 7.8°N, 134.2°W) (Figure 3q) are characterized as ISS dark areas that are extensive. Margins of this unit may show elongation in W-E direction with fingers that trend toward higher latitudes away from equator. On the boundaries of the SAR swaths, where mapped units extend beyond the borders and into the non-SAR data sets, regions of non-SAR that match the aforementioned characteristics tend to align well with mapping designated as dunes in the SAR. Radiometry shows high emissivity, similar to the linear dunes (*dl*) and the featureless sand sheets (*ds*). Undivided dunes appear dark brown in RGB VIMS, which is also similar to the appearance of the linear dunes (*dl*) and featureless sand sheets (*ds*) units. Given the low-resolution nature of non-SAR mapping, we permit less than 10% hummocky or plain terrains to be included within the mapped area.

Given their appearance in VIMS, ISS, and emissivity and their respective correlation to the characteristics expected of the dune units in these data sets, we interpret this unit as dune material deposits. Similarly, the strong directionality suggested by W-E elongation matches the material transport of dune materials and wind-swept morphology of aeolian processes (Malaska, Lopes, Hayes, et al., 2016). Subcategories of the dune unit that may be contained within the undivided dunes (*du*) include linear dunes (*dl*), reticulated dunes (*dr*), and featureless sand sheets (*ds*).

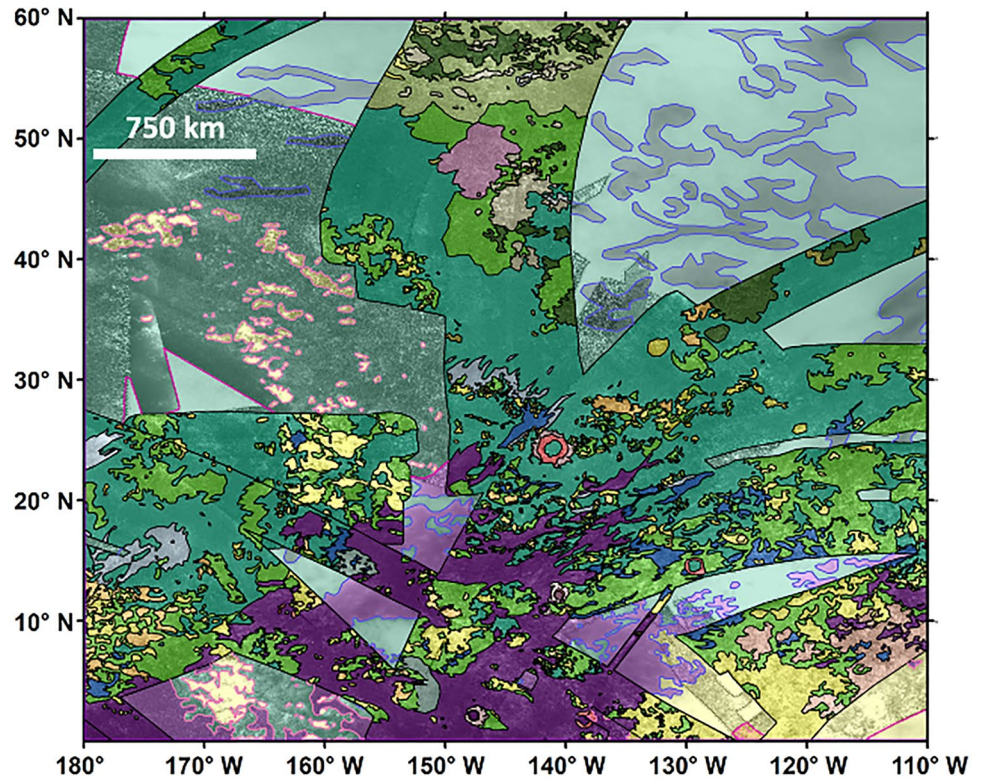
4.2.2. Undivided Hummocky/Mountainous (*hu*)

The undivided hummocky/mountainous (type area: 8.8°N, 149.2°W) (Figure 3s) appear medium-dark in ISS, bright in RGB VIMS, and radar bright in HiSAR. In radiometry, this unit shows low emissivity (~ 0.91), akin to the emissivity of the hummocky (*hh*) (~ 0.87) and mountainous (*hm*) (~ 0.90) SAR units. In some instances, this unit shows E-W linearity, while other times it is more globular or amorphous. Broad areas of the unit may contain up to 50% of other units. Areas extrapolated beyond the borders of the SAR swaths generally align with units falling under the “hummocky/mountainous” major terrain category.

We interpret this unit as encompassing the units that fall into the “hummocky/mountainous” major terrain category, which include mountains, hummocky, and pitted hummocky (*hph*) terrain units. Thus, we also interpret this unit as exposure of ancient crust, with a radiometric and spectral response consistent with fractured water ice mixed with organic material (Malaska, Lopes, Hayes, et al., 2016; Solomonidou et al., 2018). Undivided hummocky/mountainous units that are lineated in roughly the W-E direction we specifically interpret as mountain chains, although in the non-SAR and low resolution HiSAR we cannot see the bright-dark pairing in radar that is diagnostic of a mountain peak (Cook-Hallett et al., 2015; Liu et al., 2016).

4.2.3. Undivided Plains (*pu*)

The undivided plains (*pu*) (type area: 49.5°N, 167.2°W) (Figure 3t) are broad areas that appear bright in ISS and high in emissivity. This unit dominates the mid-latitudes, but it also appears in the polar and equatorial regions



Legend

Terrain Units

- mountains (*hm*)
- hummocky (*hh*)
- degraded hummocky (*hdm*)
- pitted hummocky (*hph*)
- sharpened-edged depressions (*bse*)
- ramparts (*brh*)
- crater rim (*crh*)
- crater ejecta (*ceh*)
- crater fill 3 (*cf3*)
- finely dissected labyrinths (*lbf*)

- scalloped plains (*psv*)
- variable featured plains (*pfv*)
- undifferentiated plains (*pu*)
- dark irregular plains (*pil*)
- bright gradational plains (*pgh*)
- streak-like plains (*psh*)
- featureless sand sheets (*ds*)
- dark linear dunes (*dl*)
- undivided hummocky/mountains (*hu*)
- undivided dark plains (*pdu*)
- undivided plains (*pu*)
- undivided dunes (*du*)

Contact Types

- certain
- gradational
- HiSAR boundary
- inferred
- map boundary
- approximate

Figure 7. Geomorphological map of the Soi crater region from high-resolution Synthetic Aperture Radar (SAR), high-altitude SAR (HiSAR), and non-SAR data (Radiometry, Visible and Infrared Mapping Spectrometer [VIMS], Imaging Science Subsystem [ISS], poor HiSAR). Characteristics and interpretations for each terrain unit is described in Table 1. Contact types: “certain” for units defined by SAR and “good” HiSAR; “gradational” indicates that a clear boundary could not be made at the resolution of the SAR images; “HiSAR boundary” indicates the boundary between low-resolution HiSAR and other non-SAR data sets; “Inferred” for units defined using the low-resolution HiSAR; “map boundary” to indicate the regional extent of the mapping; and “approximate” for units defined using ISS and VIMS.

Table 2
Areal Extent of Terrain Units in the Soi Crater Region

Terrain class	Terrain unit name	Number of features	Total area (km ²)	% Of mapped area (SAR and Non-SAR)	% Mapped of each terrain class
Craters	Crater ejecta (<i>ceh</i>)	5	12,348	0.18%	0.38%
	Crater rim (<i>crh</i>)	13	13,025	0.19%	
	Crater Peak (<i>cph</i>)	1	125	<0.01%	
	Crater fill 3 (<i>cf3</i>)	1	948	0.01%	
Labyrinth	Finely dissected (<i>lbf</i>)	1	32,559	0.47%	0.47%
Mountains/hummocky	Hummocky (<i>hh</i>)	624	382,233	5.46%	11.61%
	Mountain (<i>hm</i>)	95	79,336	1.13%	
	Degraded hummocky (<i>hdm</i>)	51	11,063	0.16%	
	Pitted hummocky (<i>hph</i>)	8	78,571	1.12%	
	Undivided mountains/hummocky (<i>hu</i>)	96	260,932	3.73%	
Plains	Undifferentiated plains (<i>pul</i>)	129	1,557,600	22.28%	72.64%
	Variable featured plains (<i>pfv</i>)	304	992,950	14.20%	
	Streak-like plains (<i>psh</i>)	20	72,565	1.04%	
	Scalloped plains (<i>psv</i>)	6	109,781	1.57%	
	Dark irregular plains (<i>pil</i>)	28	79,879	1.14%	
	Bright gradational plains (<i>pgh</i>)	2	24,535	0.35%	
	Undivided plains (<i>pu</i>)	59	1,907,952	27.29%	
	Undivided dark plains (<i>pdu</i>)	26	333,752	4.77%	
Dunes	Linear dunes (<i>dl</i>)	36	630,551	9.02%	14.25%
	Featureless sand sheets (<i>ds</i>)	122	115,502	1.65%	
	Undivided dunes (<i>du</i>)	25	250,582	3.58%	
Basin and lake	Sharp-edged depressions (<i>bse</i>)	60	43,079	0.62%	0.65%
	Ramparts (<i>brh</i>)	3	2,615	0.04%	

in patches broken up by the sand seas and the undivided dunes. In low resolution HiSAR, they have a medium level of backscatter, comparable to the undifferentiated plains (*pul*). Given their broad area, they may contain up to 20% of other terrain units that cannot be distinguished at the non-SAR mapping scale.

We interpret this unit as a broad plains unit that contains the plains units that appear bright in ISS, such as “undifferentiated plains,” “variable feature plains,” “scalloped plains,” etc. Given the identification of SEDs and labyrinths at the mid-latitudes, it is possible that the undivided plains may contain a certain number of either unit that cannot be resolved with the lower-resolution data sets.

4.2.4. Undivided Dark Plains (*pdu*)

The undivided dark plains (*pdu*) (type area: 45.6°N, 116.9°W) (Figure 3r) appear ISS dark, and do not cover as broad of an area as the undivided plains. In the low-resolution HiSAR, this unit has medium to variable backscatter. Similarly, this unit has varying levels of microwave emissivity, but mostly medium to high emissivity, never low (>0.95). This unit is mostly found in the mid-latitude regions and may be globular to lineated in planform.

Due to their dark appearance in ISS and their high emissivity, we interpret this unit as primarily consisting of “dark irregular plains.” However, due to their elongated form in certain mid-latitude areas this unit may also contain the elongated “streak-like plains” unit. While the “undivided dunes” also appear dark in ISS and have elongated morphology, the dunes are not expected to be found in the mid-latitude regions. It is also possible that this unit may contain a certain amount of “labyrinth” terrain, which sometimes appear dark in ISS and have high emissivity, but they cannot be resolved unambiguously (Malaska et al., 2020).

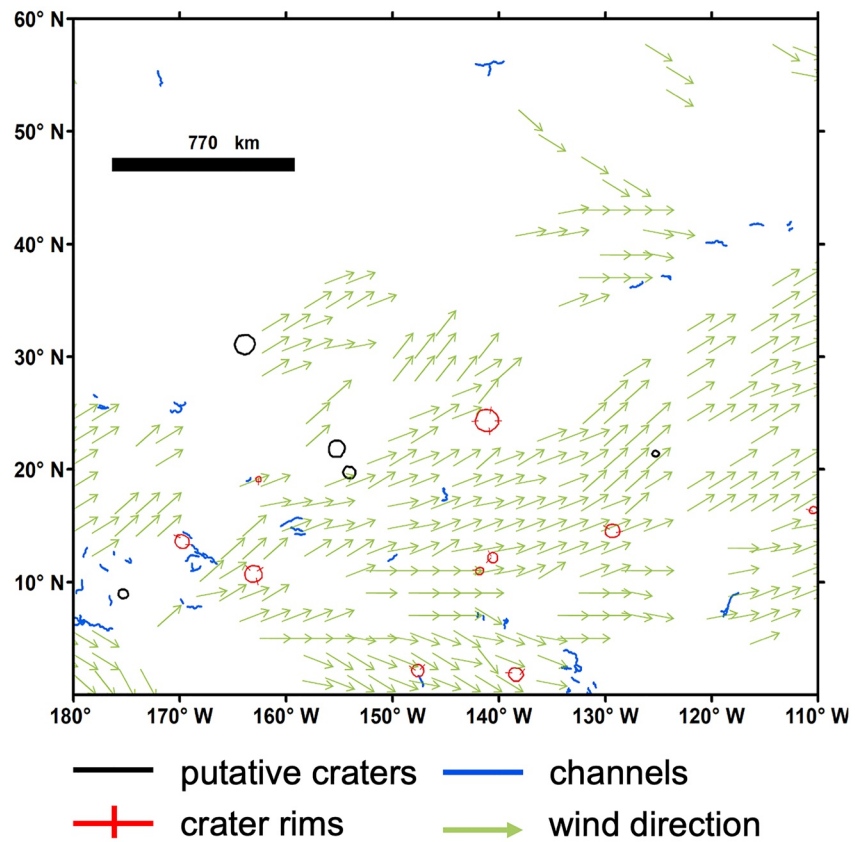


Figure 8. Sketch map of inferred material transport direction (arrows) in the Soi crater region after Malaska, Lopes, Hayes, et al. (2016), with valleys and channels (blue lines), craters (red), and putative craters (black).

Table 1 summarizes the identified terrain classes, units, and unit codes in addition to locations of characteristic examples of the units.

4.3. The Soi Crater Region Geomorphological Map

Through the combined information provided by the detailed analysis of all different types of data, including SAR and non-SAR, in addition to previous knowledge gained through the mapping of the Afekan crater region, the South Belet region, and of the global geomorphological map of Titan, we constructed the detailed geomorphological map of the Soi crater region (Figure 7). As mentioned earlier, all of the main categories of Titan units (e.g., Lopes et al., 2020) are present within the Soi crater region. Figure 7 shows the results of mapping with the use of the high-resolution SAR and HiSAR data including all available information from all Cassini surface instruments.

4.4. Terrain Unit Areal Extent

Table 2 shows the areal extent of each terrain unit in the Soi crater region. The plains units dominate the mapped area (~72.6%), consistent with the general trend around Titan's globe (see Lopes et al., 2020). The dune units are the next dominant (~14.3%), followed by mountainous terrains (~11.6%), labyrinth terrain, empty SEDs, and then craters (each of which represent less than 1% of total area). Breaking down the plains into their subunit makeup, the undivided plains make up ~27% of the mapped area, followed by the undifferentiated plains and variable featured plains, which make up ~22% and ~14% of the mapped area, respectively. Of the dune subunits, linear dunes constitute the major dune material unit (~9%), likely owing to the inclusion of part of the Shangri-La dune sea within the regional extent. Undivided dunes (~4%) and featureless sand sheets (~2%) are minor. Hummocky terrain units are the most numerous unit, but are comparatively small in terms of areal extent, with an average size of ~620 km². The undivided, scalloped, and undifferentiated plains, while not as numerous,

represent the most extensive units, with an average size of roughly 38,000, 18,000, and 13,000 km², respectively. Crater units such as rim, ejecta, and fill comprise less than 1% of the mapped surface when combined together. This is consistent with scarcity of craters on Titan's surface, likely owing to active or recently active erosional and depositional process (Crosta et al., 2021; Neish et al., 2015; Wood et al., 2010).

5. Geologic Synthesis

5.1. Surface Processes in Soi Crater Region

5.1.1. Impact Processes

We identified 10 impact craters in the Soi crater region with confidence (Table S2 in Supporting Information S1), seven of which had previously been identified by Wood et al. (2010), Neish and Lorenz (2012), Neish et al. (2015), and Hedgepeth et al. (2020). Craters identified with confidence are mapped with the crater terrain units while putative craters are mapped with a putative crater feature polyline (Figure 8). In their post-Cassini assessment of Titan's crater population, Hedgepeth et al. (2020) identified five additional crater features that we do not feel confident in identifying as craters and thus do not include as part of our geomorphological terrain map, which only includes “certain” craters. Our assessment is based on the lack of a pseudo circular or circular form of the craters in the RADAR data. Instead, we map two of these five craters as “putative craters” (black solid line) in our surface feature map (Figure 8). We additionally identify three putative craters not included in Hedgepeth et al. (2020) (Table S2 in Supporting Information S1). Many of Titan's known and suspected impact craters have been heavily eroded or modified by deposition, making interpretation subjective (Lopes et al., 2010; Neish & Lorenz, 2012; Neish et al., 2015; Wood et al., 2010). In our SAR mapping, we see examples of how dunes and dune materials invade crater interiors, breaching the rim, allowing mobile organic sands to intrude. For example, the craters located at 11°N, 141.8°W and 2°N, 147.6°W, both feature a preserved zone of crater ejecta on the eastward side of their respective rims, with the local topography presumably protecting the eastward ejecta from burial by the encroaching dunes. Both craters similarly feature substantial breaching on the western side of their rims and burial of the western-most ejecta. Furthermore, the crater floor materials are low backscatter yet contain the parallel bright-dark pairings indicative of linear dunes, suggesting that adjacent sand materials were transported from the west to the east and was able to fill the depression left behind by the initial impact.

5.1.2. Inferred Material Transport

We used alignments of streak-like plains (*psh*), featureless sand sheets (*ds*), and linear dunes (*dl*) to infer material transport directions using the method described in Malaska, Lopes, Williams, et al. (2016) and Schoenfeld et al. (2021). The inferred directions are shown in Figure 8 and are consistent with inferred global patterns. Broadly, the overall direction of material transport appears to be from the equator to mid-latitudes, along a SW to NE direction, up to latitude 35°N, then becoming roughly eastward at latitude 35°N. For latitudes above 35°N, the inferred direction of transport is from NW to SE down approximately latitude 35°N, when the inferred direction becomes roughly W to E. The alignments are interpreted to indicate sediment transport primarily by aeolian mechanisms, resulting in material being deposited at mid-latitudes (Malaska, Lopes, Hayes, et al., 2016). Local deflections of the inferred material transport vectors can be observed due to inferred topographical effects.

5.1.3. Fluvial and Aeolian Processes

5.1.3.1. Valleys and Channels

Valley and channel features are mapped (blue lines in Figure 8) using radar bright–dark pairing, networked morphology, and curvilinear appearance using the techniques and definitions in Burr, Perron, et al. (2013) and applied to the Afekan region by Malaska, Lopes, Williams, et al. (2016). Dark floored channels are more common in labyrinth terrains and mountain valleys, while bright floored channels were more often observed in the rare valleys observed within the undifferentiated plains. Valleys and channel features can only be identified if they are significantly larger than the SAR scale (Miller et al., 2021). Smaller features, such as those imaged by the Huygens probe during descent (e.g., Soderblom et al., 2007) may be present but cannot be identified at the available resolution.

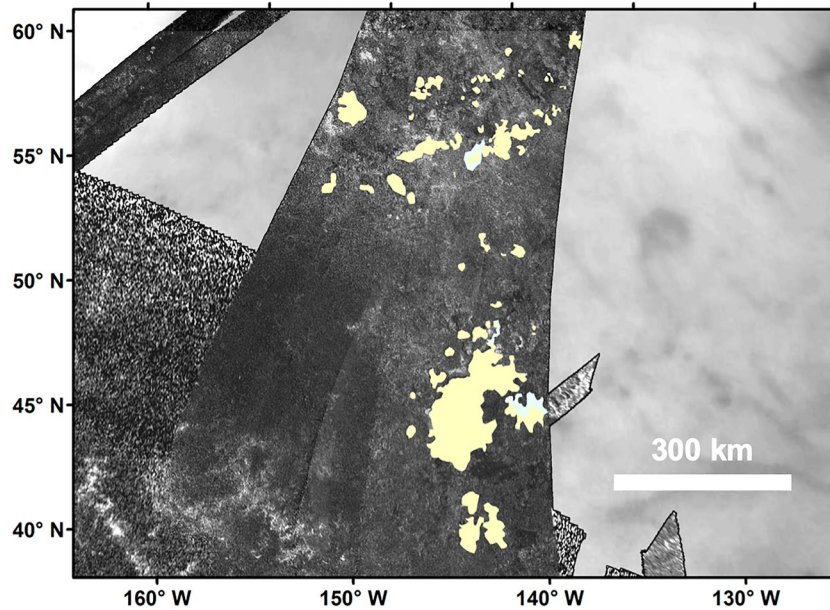


Figure 9. Mapping of all instances of Basin and Lake units in the mid-latitudes of the Soi crater region. Beige: sharp-edged depressions (*bse*); light blue-gray: ramparts (*brh*).

5.1.3.2. Gradational Versus Streak-Like Plains

We find that the bright gradational plains, a unit we discuss in Section 4.1.1, possess signatures very similar to the bright streak-like plains (*psh*) across all the mapping data sets. The streak-like plains are characterized as radar-bright features with diffuse internal texture with elongated morphology (Malaska, Lopes, Williams, et al., 2016). The elongation of this terrain unit has been observed extending in directions parallel to nearby linear dunes, suggesting that the streak-like plains represent material that has been transported and deposited by aeolian means. Both *pgh* and *psh* appear bright in radar, with diffuse internal texture (Figures 4a and 4f). Their microwave emissivity is comparable, and both appear to have lower microwave emissivity than the undifferentiated plains (*pul*) or variable feature plains (*pfv*) (Figures 4d and 4i). In VIMS maps by Le Mouélic et al. (2019), both units appear “blue” (Figures 4c and 4h), and in ISS both units appear generally darker than surrounding bright plains (although the bright gradational plains can be patchy and variable) (Figures 4b and 4g).

Due to the aforementioned characteristics, we interpret the bright gradational plains as high backscatter materials originating from the icy hummocky materials. Their orientation and directions can then reflect one of two scenarios: (a) they are aeolian sediments; (b) they are fluvial sediments that have been cleared off by winds. Similarly, in Malaska, Lopes, Williams, et al. (2016), the bright streak-like plains have been interpreted as fluvially derived materials subjected to aeolian transport, generally following inferred downwind directions. However, an alternative to a deposit of streak-like material would be the removal or scouring of material to reveal a deeper icy substrate. Due to their similar signatures across all utilized mapping data set despite differing planform morphologies, we propose that the bright streak-like plains and the bright gradational are two endmembers of the same fundamental feature, reflecting either dominantly fluvial or aeolian transport. Where the bright gradational plains result in lobate, fan-like structure, we favor a fluvial origin. Meanwhile, the bright streak-like plains are linear and structured, suggesting downwind aeolian deposition or directed scouring. We propose that the initial grain forming process was fluvial erosion of either an organic or icy substrate, but that the final deposition of the fine-grained sediment was either through fluvial or aeolian means. The dominant process determines the endmember morphology, resulting in either a fluvial lobate (*pgh*) unit or an aeolian streak-like (*psh*) unit.

5.1.4. Lacustrine Processes and the Mid-Latitude Plains

In our mapping of the Soi crater region, we identified 60 features consistent in size and morphology to the polar SEDs, which we also refer to as SEDs (*bse*) (Figure 5). The spatial extent of these features reaches as far south as 40°N (Figure 9). Additionally, remapping of Afekan's mid-latitudes has revealed 31 features that are morphologically

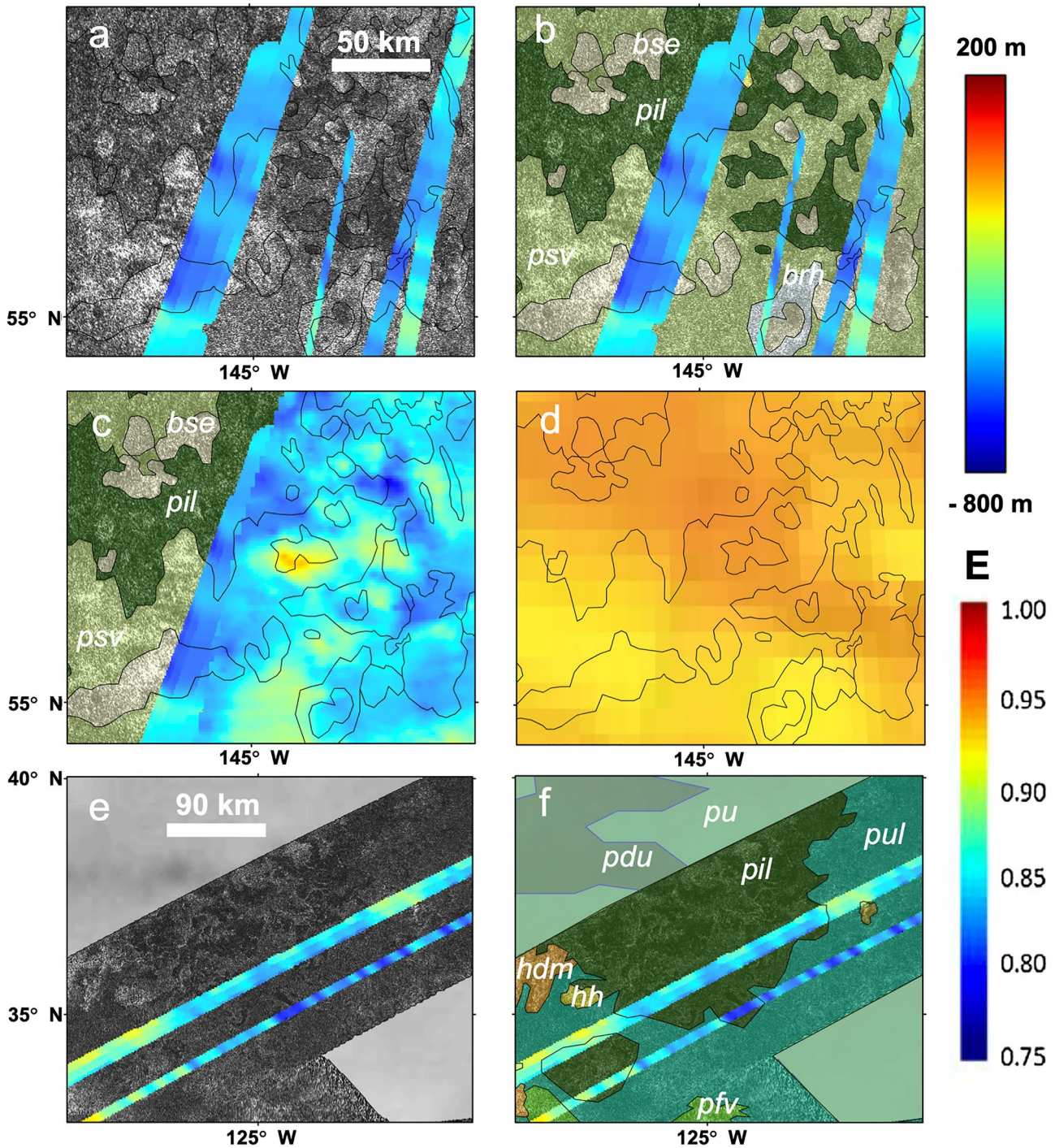


Figure 10. The dark irregular plains (*pil*) and their relationship to the sharp-edged depressions (*bse*). (a) Topography from SARTopo of northern reach of the Soi crater region *pil*; panel (b) same as panel (a) with the annotated terrain unit mapping as background; (c) Digital Terrain Model of northern part of the Soi crater region showing topographic highs among *pil*; (d) emissivity map covering area shown in panels (a–c); (e) SARTopo with Synthetic Aperture Radar as background and annotated unit map (f) of the largest patch of dark irregular plains in the Soi crater region, showing large topographic lows.

consistent with the SEDs (Figure 5h), extending to 48°N. Using available elevation data (SARTopo, DTM for 46 out of 60 SEDs), the majority of the depressions seen in the Soi crater region have flat floors, to within 100 m certainty, consistent with observations of empty depressions in the polar regions (A. G. Hayes et al., 2017; Birch et al., 2017). However, the largest of the SEDs we identify have more complex floor topography (i.e.,

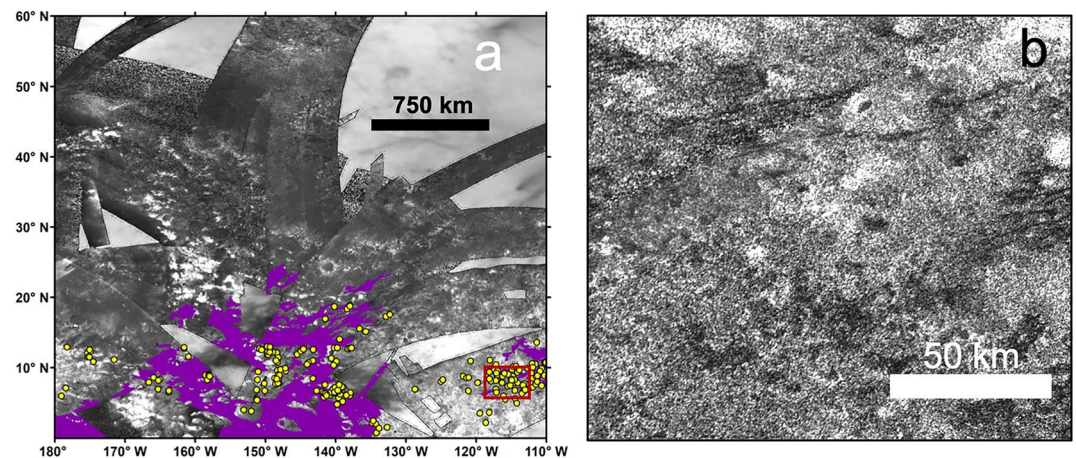


Figure 11. Equatorial pits in the Soi crater region (yellow dots). (a) Pit mapping in the Synthetic Aperture Radar, with the dune fields (in purple) also lit up. (b) Zoom in of area marked by red square in panel (a), centered on 8.9°N, 115.3°W.

terraced), potentially indicating either a higher degree of fluvial/aeolian desiccation, or coalescence of multiple smaller depressions (A. G. Hayes et al., 2017). We interpret the *bse* units in the Soi crater region as now empty lake basin, indicating that processes previously thought as “polar” were once operating in the mid-latitudes, suggesting a once wetter Titan.

Three of the SEDs, or empty lakes, in Soi crater region have an associated rampart, supporting the hypothesis that the ramparts are features that formed as part of the lake emplacement, but are progressively eroded away. Thus only the youngest lakes would still possess their ramparts (Solomonidou, Le Gall, et al., 2020), explaining their scarcity. Nonetheless, the identification of ramparts in the Soi crater region reinforce the idea that the mid-latitude lakes formed and evolved in much that same way as the polar lakes.

The SEDs are found adjacent to two other units unique to the mid-latitudes of Titan: the scalloped plains (*psv*) and the dark irregular plains (*pil*) (Figure 10). These two units in particular seem to define the morphology of Titan's mid-latitude-to-pole transitional zones and have been identified in the northern (Lopes et al., 2020; Malaska, Lopes, Williams, et al., 2016) and southern hemispheres (Schoenfeld et al., 2021). Topographically, the scalloped plains undulate, but typically appear elevated with respect to the dark-irregular plains and the SEDs (Figures 10b and 10c). Additionally, the scalloped plains appear radiometrically distinct, having a lower emissivity (0.93–0.94) from the dark irregular plains (0.97–0.98) (Figure 10d). These observations are consistent with the interpretation of the scalloped plains being either a thick organic layer mixed with higher dielectric constant materials, or as a more textured surface of the organics typical of the undifferentiated plains, with higher backscatter due to more surface roughness. Furthermore, VIMS analyses agrees with the organic nature of the top surfaces of *psv* (Solomonidou et al., 2018).

The topography of the dark irregular plains (*pil*), and their relationship to the SEDs (*bse*), appear more complicated. Previous work (e.g., Malaska, Lopes, Williams, et al., 2016; Schoenfeld et al., 2021; Stofan et al., 2007) interpreted the dark irregular plains as consisting of local basins dampened by liquid hydrocarbons pooling in either the surface or the near-subsurface. The Huygens probe, for example, detected a surface damp with hydrocarbon liquids upon touchdown (Lorenz, Niemann, et al., 2006). These areas could be transient ponds that have mostly evaporated, leaving behind remnant liquids that continue to wet sediments. Precipitation events, as evidences by surface brightness changes in VIMS/ISS (Barnes et al., 2013), may be responsible for such transient wetting. Alternatively, the liquid may have infiltrated downward, but left behind locally damp material, if we assume a low evaporation rate. Based on laboratory measurements (e.g., Grundy et al., 2002), it is possible that methane exists on Titan's surface as a liquid mixed with other ices, possibly filling the space between their grains. Remnant liquids are possibly composed of higher order hydrocarbons, including ethane, propane, and perhaps even 1-butene; these hydrocarbons would be more refractory than methane and could therefore create remnant damp sediment even after the more volatile methane has evaporated (Cordier et al., 2016; Malaska & Hodyss, 2014). Another possibility is that low backscatter is from very fine-grained material that has been sorted

and redeposited, again, from localized transient ponding (Turtle et al., 2011). In suspension, the material would fine upwards.

While some of the dark irregular plains are indeed the lowest feature along a topographic trace, this is not always the case. Some of the dark irregular plains observed in the Soi crater region are topographic highs (Figures 9b and 9c), especially with respect to the lakes (*bse*). While this is inconsistent with our prior interpretation, it is possible we may be seeing two different terrain types that have broadly been classified as dark irregular plains owing to their similarity in radar and other supplementary data sets. However, topographic data over SAR-dark features is less reliable (Corlies et al., 2017), and so relative elevations of these features may be particularly skewed. Future analyses may split these terrains out into two separate categories, yet still falling under the major plains terrain class. The topographically higher dark irregular plains adjacent to the SEDs may be remnant highs left over from lake aggregation, similar to what is observed at the poles (Birch et al., 2017). Thus, their dark appearance in radar may be owing to low-backscatter materials, rather than near-surface wetting. The dark irregular plains that do sit lower than nearby empty lakes, however, may in fact represent wetted lowlands, or at least represent the sites of localized ponding. The largest patch of dark irregular plains in the Soi crater region, for example, sits at 37°N, and represents a large topographic low (Figures 10e and 10f). The dark irregular plains that are lower than the empty lakes may be approaching or interfacing with the phreatic surface of the methane table no longer accessible by the now empty lakes, consistent with predictions from global circulation models of Titan's climate (e.g., Faulk et al., 2020). Or, the dark irregular plains may be the result of higher precipitation/humidity with increasing latitude interacting with porous regolith and local topography to create ephemeral surface and near surface wetting.

5.1.5. Equatorial Pits in the Soi Crater Region

Within the Soi crater regional map, there are numerous radar dark, circular features with diameters ranging in size from about 1 to 6 km. In total, 230 of these features were identified (Figure 11). Similar features of this specific morphology, assumed to be depressions or pits, were first identified by Lopes et al. (2007) within Cassini's T8 swath, and were similarly mapped in the South Belet region (Schoenfeld et al., 2021). The size range of the Soi crater region pits is similar to that of South Belet and the T8 pits, with a similar level of random distribution within a given location. We thus interpret the pits of the Soi crater region to have formed in the same manner as the pits found in the T8 SAR swath and in South Belet. As a note, we only use the highest resolution SAR to map the pits (Figure 11b).

The equatorial pits primarily occur within large areas of exposed crust; this association is the qualitative basis behind distinguishing “pitted hummocky” (*hph*) from regular “hummocky” (*hh*). It could be that, being locally elevated to the surrounding terrain, pitted depressions are preserved from complete burial by windward sediments and incidentally become associated with mountains and hummocks. Alternatively, it could be a contrast effect, where backscatter afforded by the radar bright hummocky terrain makes the pits easier to identify. Within the Soi crater region, collections of pits are particularly dense in areas adjacent to dune fields (Figure 11a). This observation is consistent with our past interpretation (e.g., Schoenfeld et al., 2021) of the pits as wind-blown organic sands deposited and concentrated into pre-existing depressions within exposure of the ancient ice crust. In particular, the highest concentration of pits occurs within the northwestern margin of Xanadu that overlaps into the Soi crater region, which is also down-wind to a large dune field. The ubiquity of pits in equatorial regions may then be owing to the prevalence of both mountainous regions and dune fields at these latitudes, as opposed to a formation mechanism limited to equatorial areas. The ancient crust of Titan, therefore, may be pocked and pitted by processes separate from cratering, as the morphologies and size distributions of these pits are not consistent with those of impact craters (e.g., Lopes et al., 2007; Lunine et al., 2008). Schoenfeld et al. (2021) hypothesizes that the equatorial pits may have formed as a result of either cryovolcanism, the removal of methane (either from outgassing or the retreat of a ground reservoir) in the near surface, or as a result of the dissolution of soluble organics in an otherwise icy matrix. Eventually, the pits were infilled with windward dune material.

6. Geologic History

The goal of this paper is to create a geomorphological terrain map of the Soi crater region, in order to better understand the geologic evolution of the region, as well as offers a complementary data set for compositional analysis (e.g., Solomonidou et al., 2018). We identified 22 geomorphological units in the Soi crater region, 3 of which not previously described in our mapping. Some newly identified features include 60 SEDs, which reach as far south as 40°N. We also introduce three impact craters to the literature. The Soi crater region contains the NE section of Shangri-La dune field, a vast field of equatorial dunes at lower latitudes, part of the Xanadu region, and also large expanses of plains at mid-latitudes.

The Soi crater region is representative of the transition between the equatorial, mid-latitude, and high latitude northern regions of Titan and largely has the same collection and proportion of geomorphological units (plains, dunes, hummocky/mountains) to other mapped regions on Titan (Lopes et al., 2020; Malaska, Lopes, Williams, et al., 2016; Schoenfeld et al., 2021). The results of this study further support the hypothesis that surface processes are, broadly speaking, the same around Titan's middle and equatorial latitudes, with the notable exception of the equatorial Xanadu region. Only at higher latitudes do these trends begin to change, as evidenced by morphologies suggestive of lacustrine processes in the Soi crater region.

The mountainous units are interpreted as the oldest unit, the undifferentiated plains are of intermediate age, and the dune are the youngest. We also consider the SEDs and the ramparts units to be some of the youngest in the Soi crater region, having printed into the plains. That said, active lacustrine processes seem to no longer operate in the mid-latitudes, as is evident by the lack of filled lakes. Solomonidou, Le Gall, et al. (2020) showed that the ramparts and the floors of the empty lakes are of the same composition. They furthermore suggest that during or after the formation of the lake basin, residual material is built into the raised rim feature and develops later into the ramparts. Lakes retaining a complete rampart structure around their circumference may be younger compared to other lakes with incomplete or degraded ramparts, which are further along in the process of having their ramparts eroded away.

Topography data acquired from DTMs and SARTopo shows that the mountainous terrains are topographically higher, and the dunes are lower. The Soi crater region presents similar bulk geomorphology as the rest of Titan's surface, which is rich in plains and dunes. The plains cover 3/4 of the region, of which half is the undivided plains and the undifferentiated plains. While the undivided plains unit dominate the mid-latitude region of the Soi crater region, there are likely other subunits contained therein, unresolved at the nonSAR scale. There are plenty of exposures of mountainous terrains around the region, but they do not cover a significant amount of the surface, in contrast to the undivided and undifferentiated plains that cover almost half of the Soi crater region. Dune materials cover ~14% of the area, which is less than what is seen in other mapped regions like the South Belet and Afekan regions (Malaska, Lopes, Williams, et al., 2016; Schoenfeld et al., 2021). The SEDs, the ramparts, and the crater units combined comprise around 1% of the mapped surface.

The identification of lakes (SEDs) outside of the polar regions and into the mid-latitudes strengthens the argument that in Titan's past, lacustrine processes typically associated with the polar regions were operating long enough to leave behind surface expressions consistent with lacustrine processes (e.g., Barnes et al., 2011; Birch et al., 2018; Hofgartner et al., 2020; MacKenzie et al., 2014; Turtle et al., 2009). Previous studies have proposed that features in Tui and Hotei Regio, located at equatorial latitudes, are morphologically and topographically consistent with the polar empty lakes (Moore & Howard, 2010). Additionally, global distribution of evaporitic features places a high areal concentration of the associate 5- μ m bright signal within these same basins (MacKenzie et al., 2014). We can similarly conclude that the substrate of the mid-latitudes support the formation of lacustrine features, much like the polar regions, and perhaps may be the same underlying material. Furthermore, their presence speaks to a wetter climate, where the mid-latitudes were once as humid as the poles (e.g., Moore et al., 2014). Alternatively, we may consider a scenario where the climate is unchanged (over the lifetime of the lakes), but that frequency of rain is less at these latitudes such that abundance of filled lake features is less. It is predicted that total precipitation for Titan are largest over the poles when compared to the mid-latitudes (e.g., Faulk et al., 2017). However, there are several lines of evidence that favor the hypothesis of a desiccating Titan. For one, there is the issue of methane being progressively lost over time (e.g., Larsson & McKay, 2013; Moore et al., 2014), as a result of photodissociation in the upper atmosphere, conversion to solid organics, or incorporation into clathrate. While there may be periods of methane outgassing and atmospheric replenishment, there is nonetheless net loss and humidity recedes

to the poles. Within the north pole, evidence of such loss is observed: empty SEDs located adjacent to filled lakes sit at slightly higher elevations (A. G. Hayes et al., 2017), presumably having been filled during a previous epoch with larger liquid inventories (Birch et al., 2017). Similarly, the rounded lakes are thought to form on geologic timescales (e.g., Birch et al., 2017), requiring time for them to imprint onto the landscape. Thus, the timescale of interaction with a liquid-methane reservoir was such that lakes consistent in size, complexity, and frequency with that of the poles were once operating in the mid-latitudes. However, if the initial depression was formed by other means, that is, maar-like explosion (e.g., Mitri et al., 2019), then this argument may not apply. That said, the morphology of the lake boundaries as rounded with sharp shorelines and no associated inflow channels (at least not at Cassini resolution) are consistent with seepage lakes interacting with a local ground-methane system, as opposed to runoff from precipitation (A. Hayes et al., 2008).

Craters appear to get filled with aeolian material and eventually are buried, which could explain the relatively few number of craters on Titan (e.g., Hedgepeth et al., 2020; Neish et al., 2015, 2016; Wood et al., 2010). The craters located close to the equator (including Santorini) appear organic in composition, as they are rich in the dark organic material and tholin-like material, without the presence of any water ice (Solomonidou, Neish, et al., 2020). The Soi crater rim and ejecta appears primarily composed of tholin-like material, followed by water-ice, a mixture that is characteristic of the plains craters located around the 30°N latitude zone (Solomonidou, Neish, et al., 2020). The Soi crater region impact craters offer good examples of dune material “invading” the interior of the craters.

In terms of surface area, the scalloped plains unit is of minor importance in the Afekan crater region but is extensive in the Soi crater region. This unit, as well as the dark irregular plains, appear to be transitional between the aeolian-dominated mid-latitudes and the fluvially-dominated polar regions, where aeolian deposition is scarce. Hence, the scalloped (*psv*) and dark irregular plains (*pil*), both of which are found adjacent to the SEDs (*bse*) in the Soi crater region, seem to play a major role in defining the morphology of Titan's mid-latitude-to-pole transitional zones. These three units occupy the middle northern part of the Soi crater region. The scalloped plains are topographically higher than the other two units. We suggest that the northern *pil* close to the SEDs are remnant highs left over from lake aggregation similarly to the ramparts; dark irregular plains that sit in topographic lows alternatively may represent near-surface wetting by ground methane.

7. Conclusion

We have presented and described a geomorphologic map of the Soi crater region of Titan. We used Cassini SAR as our basemap, supplemented with other data sets such as radiometry, topography, ISS, and VIMS. This entire region makes up ~10% of Titan's areal surface, whereas the parts of the region imaged by SAR make up ~5.6% of Titan's surface. This area represents the main geological processes that have occurred in Titan's equatorial and the northern mid-latitudes. We describe in detail three new mapping units: the “bright gradational plains,” “SEDs,” and “ramparts.” These units have been identified elsewhere on Titan and have been described in the literature. Here, we discuss them in the context of the Soi crater region and incorporate them into our mapping schema, building on the work presented in Malaska, Lopes, Williams, et al. (2016) and Schoenfeld et al. (2021). We also use the correlation between Cassini SAR and secondary data sets to map into areas not imaged by SAR, elaborating on a methodology for a more comprehensive map of Titan's surface (first introduced in Lopes et al., 2020). Additionally, we use lower resolution HiSAR for the low-resolution mapping. In the Soi crater region, these “nonSAR” units included undivided dunes (*du*), undivided hummocky (*hu*), undivided plains (*pu*), and undivided dark plains (*pdu*).

The Soi crater region contains all six of the main terrain units: Dunes, Plains, Mountain/hummocky, Crater, Labyrinths, and the Basin and Lake units. We find that plains dominate the make-up of this region, accounting for 72.6% of the mapped area, followed by dunes (14.2%), mountains/hummocky terrains (11.6%), labyrinth (0.47%), basin and lake (0.65%), and crater terrains (0.38%). The emissivity and spectral properties of the undifferentiated plains and dunes are consistent with organic materials, whereas the emissivity and spectral properties of the mountain/hummocky and crater terrains are more consistent with water ice. We identify 10 impact craters in the Soi crater region with confidence, seven of which have been identified in the literature.

Broadly, the geologic history of the Soi crater region presents a story familiar to that of the Afekan crater region and South Belet, but with some notable differences. We observe small instances of fluvial transport in the Soi

crater region in the form of channels. Instead, material transport patterns are more consistent with widespread aeolian deposition of dunes and plains units. If fluvial activity was once more present in this region, it has since been buried by aeolian deposits. However, we interpret the bright gradational plains (*pgh*) as high backscatter material originating from fluvial processes, representing a fluvially derived depositional units. They are similarly found in association with mapped channels in both the Soi crater region and in other regions (Figure 4k). We also find that the bright gradational plains possess signatures very similar to the bright streak-like plains (*psh*) across all the mapping data sets. Accordingly, we propose that the bright streak-like plains and the bright gradational are two endmembers of the same fundamental feature, reflecting either dominantly fluvial or aeolian transport. The dominant process determines the endmember morphology, resulting in either a fluvial lobate (*pgh*) unit or an aeolian streak-like (*psh*) unit.

The identification of lake units in the Soi crater region, the SEDs (*bse*) and ramparts (*brh*), challenges the idea of lacustrine processes being limited to Titan's polar regions, suggesting a historically wetter Titan (e.g., Aharonson et al., 2009; Birch et al., 2018; MacKenzie et al., 2014; Neish et al., 2013). The amount of methane in the atmosphere and on the surface may have changed over time, resulting in a complex interplay of the hydrocarbon "aquifer" level. During a base-level lowering, depressions sitting at the highest elevation would be abandoned first, losing their connection to the receding methane aquifer (A. G. Hayes et al., 2017). The spatial extent of these features in the Soi crater region reaches as far south as 40°N. Additionally, remapping of Afekan's mid-latitudes has revealed 31 features that are morphologically consistent with the SEDs, suggesting that the prevalence of empty lakes at those latitudes is not necessarily unique to the Soi crater region. The morphology and complexity of the Soi SEDs are consistent with observations of empty depressions in the polar regions (A. G. Hayes et al., 2017; Birch et al., 2017), suggesting a shared formation history, including instances of smaller depressions coalescing.

The SEDs are found adjacent to two other units unique to the mid-latitudes of Titan: the scalloped plains (*psv*) and the dark irregular plains (*pil*) (Figure 9). Some of the dark irregular plains observed in the Soi crater region are topographic highs, while some are the lowest feature along a topographic trace, including with respect to the lakes (*bse*). While this is inconsistent with our prior interpretation of the dark irregular plains as consisting of local basins dampened by liquid hydrocarbons pooling in either the surface or the near-subsurface, it is possible we are seeing two different terrain types that have broadly been classified as dark irregular plains. The topographically higher dark irregular plains adjacent to the SEDs may be remnant highs left over from lake aggregation, similar to what is observed at the poles (Birch et al., 2017). Thus, their dark appearance in radar may be owing to a more absorptive material, rather than near-surface wetting. The dark irregular plains that do sit lower than nearby empty lakes, however, may in fact represent wetted lowlands. The dark irregular plains that are lower than the empty lakes may be approaching or interfacing with the phreatic surface of the methane table.

Our geomorphological mapping results for the Soi crater region is consistent with the narrative of Titan's equatorial and mid-latitudes being dominated by organic materials that have been deposited and emplaced by aeolian activity. Additionally, the presence of similar units found in both Afekan, South Belet, and Soi suggests latitudinal symmetry in Titan's surface processes and their evolution across a broad longitudinal spread.

Data Availability Statement

All *Cassini* data used in this article can be accessed in the Planetary Data Systems (PDS) Image Atlas (https://pds-imaging.jpl.nasa.gov/search/?fq=ATLAS_MISSION_NAME%3Acassini%26fq=TARGET%3Atitan%26fq=-ATLAS_THUMBNAIL_URL%3Abrwsnotavail.jpg%26fq=ATLAS_INSTRUMENT_NAME%3Aradar%26q=%3A*). The detailed product IDs for RADAR can be found in Table S1 in Supporting Information S1. Our geomorphological mapping was done using ArcGIS (ESRI) software version 10.6 (<https://www.esri.com/en-us/arcgis/about-arcgis/overview>). RADAR DOI: Stiles (2017a), <https://doi.org/10.17189/1520231>. SARTopo DOI: Stiles (2017b), <https://doi.org/10.17189/1520238>. Altimeter DOI: Alberti (2017), <https://doi.org/10.17189/1520209>. All shapefiles created as part of this mapping campaign, including terrain units, contacts, surface features, pit distribution, and mapping boundaries can be found at Schoenfeld (2022).

Acknowledgments

The authors wish to thank the entire Cassini RADAR Team and the Cassini mission scientists and engineers for their hard work that made this exploration possible. RADAR DOI: Stiles (2017a), <https://doi.org/10.17189/1520231>. SARTopo DOI: Stiles (2017b), <https://doi.org/10.17189/1520238>. Altimeter DOI: Alberti (2017), <https://doi.org/10.17189/1520209>. AMS was supported by an NSF graduate student fellowship, Grant DGE-1650604. This research was partly supported by the NASA Astrobiology Institute through its JPL-led project entitled Habitability of Hydrocarbon Worlds: Titan and Beyond. This research was partly supported by the Cassini Data Analysis and Participating Scientists Program (CDAPS) Grant NH16ZDA001N to R.L. A.S. acknowledges support from the CNES Appel annuel à Propositions de Recherche Program. A.S. was partly supported by the Czech Science Foundation (Grant 20-27624Y). S.P.D.B. acknowledges support from the Heising-Simons Foundation (51 Pegasi b Fellowship). This work was conducted at the Jet Propulsion Laboratory (JPL) and the California Institute of Technology (Caltech) under contract with the NASA. © 2022 California Institute of Technology. Government sponsorship acknowledged.

References

- Aharonson, O., Hayes, A. G., Lunine, J. I., Lorenz, R. D., Allison, M. D., & Elachi, C. (2009). An asymmetric distribution of lakes on Titan as a possible consequence of orbital forcing. *Nature Geoscience*, 2(12), 851–854. <https://doi.org/10.1038/ngeo698>
- Alberti, G. (2017). Cassini orbiter radar altimeter burst data record summary. Planetary Data System V1. <https://doi.org/10.17189/1520209>
- Barnes, J. W., Bow, J., Schwartz, J., Brown, R. H., Soderblom, J. M., Hayes, A. G., et al. (2011). Organic sedimentary deposits in Titan's dry lakebeds: Probable evaporite. *Icarus*, 216(1), 136–140. <https://doi.org/10.1016/j.icarus.2011.08.022>
- Barnes, J. W., Brown, R. H., Soderblom, L., Sotin, C., Le Mouëlic, S., Rodriguez, S., et al. (2008). Spectroscopy, morphometry, and photoclinometry of Titan's dunefields from Cassini/VIMS. *Icarus*, 195(1), 400–414. <https://doi.org/10.1016/j.icarus.2007.12.006>
- Barnes, J. W., Buratti, B. J., Turtle, E. P., Bow, J., Dalba, P. A., Perry, J., et al. (2013). Precipitation-induced surface brightenings seen on Titan by Cassini VIMS and ISS. *Planetary Science*, 2(1), 1–22. <https://doi.org/10.1186/2191-2521-2-1>
- Barnes, J. W., Radebaugh, J., Brown, R. H., Wall, S., Soderblom, L., Lunine, J., et al. (2007). Near-infrared spectral mapping of Titan's mountains and channels. *Journal of Geophysical Research*, 112(E11), E11006. <https://doi.org/10.1029/2007JE002932>
- Birch, S. P. D., Hayes, A. G., Corlies, P., Stofan, E. R., Hofgartner, J. D., Lopes, R. M. C., et al. (2018). Morphological evidence that Titan's southern hemisphere basins are paleoseas. *Icarus*, 310, 140–148. <https://doi.org/10.1016/j.icarus.2017.12.016>
- Birch, S. P. D., Hayes, A. G., Dietrich, W. E., Howard, A. D., Bristow, C. S., Malaska, M. J., et al. (2017). Geomorphologic mapping of Titan's polar terrains: Constraining surface processes and landscape evolution. *Icarus*, 282, 214–236. <https://doi.org/10.1016/j.icarus.2016.08.003>
- Birch, S. P. D., Hayes, A. G., Howard, A. D., Moore, J. M., & Radebaugh, J. (2016). Alluvial fan morphology, distribution and formation on Titan. *Icarus*, 270, 238–247. <https://doi.org/10.1016/j.icarus.2016.02.013>
- Birch, S. P. D., Hayes, A. G., Poggiali, V., Hofgartner, J. D., Lunine, J. I., Malaska, M. J., et al. (2019). Raised rims around Titan's sharp-edged depressions. *Geophysical Research Letters*, 46(11), 5846–5854. <https://doi.org/10.1029/2018gl078099>
- Bratsolis, E., Bampasidis, G., Solomonidou, A., & Coustenis, A. (2012). A despeckle filter for the Cassini synthetic aperture radar images of Titan's surface. *Planetary and Space Science*, 61(1), 108–113. <https://doi.org/10.1016/j.pss.2011.04.003>
- Brossier, J. F., Rodriguez, S., Cornet, T., Lucas, A., Radebaugh, J., Maltagliati, L., et al. (2018). Geological evolution of Titan's equatorial regions: Possible nature and origin of the dune material. *Journal of Geophysical Research: Planets*, 123(5), 1089–1112. <https://doi.org/10.1029/2017je005399>
- Burr, D. M., Drummond, S. A., Cartwright, R., Black, B. A., & Perron, J. T. (2013). Morphology of fluvial networks on Titan: Evidence for structural control. *Icarus*, 226(1), 742–759. <https://doi.org/10.1016/j.icarus.2013.06.016>
- Burr, D. M., Jacobsen, R. E., Roth, D. L., Phillips, C. B., Mitchell, K. L., & Viola, D. (2009). Fluvial network analysis on Titan: Evidence for subsurface structures and west to east wind flow, southwestern Xanadu. *Geophysical Research Letters*, 36(22), L22203. <https://doi.org/10.1029/2009GL040909>
- Burr, D. M., Perron, J. T., Lamb, M. P., Iriwin, R. P., III, Collins, G. C., Howard, A. D., et al. (2013). Fluvial features on Titan: Insights from morphology and modeling. *The Geological Society of America Bulletin*, 125(3–4), 299–321. <https://doi.org/10.1130/B30612.1>
- Clark, R. N., Curchin, J. M., Barnes, J. W., Jaumann, R., Soderblom, L., Cruikshank, D. P., et al. (2010). Detection and mapping of hydrocarbon deposits on Titan. *Journal of Geophysical Research*, 115(E10), E10005. <https://doi.org/10.1029/2009JE003369>
- Cook-Hallett, C., Barnes, J. W., Kattenhorn, S. A., Hurford, T., Radebaugh, J., Stiles, B., & Beuthe, M. (2015). Global contraction/expansion and polar lithospheric thinning on Titan from patterns of tectonism. *Journal of Geophysical Research: Planets*, 120(6), 1220–1236. <https://doi.org/10.1002/2014JE004645>
- Cordier, D., Cornet, T., Barnes, J. W., MacKenzie, S. M., Le Bahers, T., Nna-Mvondo, D., et al. (2016). Structure of Titan's evaporites. *Icarus*, 270, 41–56. <https://doi.org/10.1016/j.icarus.2015.12.034>
- Corlies, P., Hayes, A. G., Birch, S. P. D., Lorenz, R., Stiles, B. W., Kirk, R., et al. (2017). Titan's topography and shape at the end of the Cassini mission. *Geophysical Research Letters*, 44(23), 11754–11761. <https://doi.org/10.1002/2017GL075518>
- Coutelier, M., Cordier, D., Seignover, B., Rannou, P., Le Gall, A., Cours, T., et al. (2021). Distribution and intensity of water ice signature in South Xanadu and Tui Regio. *Icarus*, 364, 114464. <https://doi.org/10.1016/j.icarus.2021.114464>
- Crosta, A., Silber, E., Lopes, R., Johnson, B., Bjonnes, E., Malaska, M., et al. (2021). Modeling the formation of Menrva impact crater on Titan: Implications for habitability. *Icarus*, 370, 114679. <https://doi.org/10.1016/j.icarus.2021.114679>
- Elachi, C., Wall, S., Allison, M., Anderson, Y., Boehmer, R., Callahan, P., et al. (2005). Cassini radar views the surface of Titan. *Science*, 308(5724), 970–974. <https://doi.org/10.1126/science.1109919>
- Elachi, C., Wall, S., Janssen, M., Stofan, E., Lopes, R., Kirk, R., et al. (2006). Titan radar mapper observations from Cassini's T3 fly-by. *Nature*, 441(7094), 709–713. <https://doi.org/10.1038/nature04786>
- Faulk, S., Lora, J., Mitchell, J., & Milly, P. (2020). Titan's climate patterns and surface methane distribution due to the coupling of land hydrology and atmosphere. *Nature Astronomy*, 4, 390–398. <https://doi.org/10.1038/s41550-019-0963-0>
- Faulk, S., Mitchell, J., Moon, S., & Lora, J. (2017). Regional patterns of extreme precipitation on Titan consistent with observed alluvial fan distribution. *Nature Geoscience*, 10(11), 827–832. <https://doi.org/10.1038/ngeo3043>
- Greeley, R., & Batson, R. M. (1990). *Planetary mapping*. Cambridge University Press.
- Grundy, W. M., Schmitt, B., & Quirico, E. (2002). The temperature-dependent spectrum of methane ice I between 0.7 and 5 μm and opportunities for near-infrared remote thermometry. *Icarus*, 155(2), 486–496. <https://doi.org/10.1006/icar.2001.6726>
- Hayes, A., Aharonson, O., Callahan, P., Elachi, C., Gim, Y., Kirk, R., et al. (2008). Hydrocarbon lakes on Titan: Distribution and interaction with a porous regolith. *Geophysical Research Letters*, 35(9), L09204. <https://doi.org/10.1029/2008GL033409>
- Hayes, A. G., Birch, S. P. D., Dietrich, W. E., Howard, A. D., Kirk, R. L., Poggiali, V., et al. (2017). Topographic constraints on the evolution and connectivity of Titan's lacustrine basins. *Geophysical Research Letters*, 44(23), 11–745. <https://doi.org/10.1002/2017gl075468>
- Hayes, A. G., Lorenz, R. D., & Lunine, J. I. (2018). A post-Cassini view of Titan's methane-based hydrologic cycle. *Nature Geoscience*, 11(5), 306–313. <https://doi.org/10.1038/s41561-018-0103-y>
- Hedgepeth, J. E., Neish, C. D., Turtle, E. P., Stiles, B., Kirk, R., & Lorenz, R. D. (2020). Titan's impact crater population after Cassini. *Icarus*, 344, 113664. <https://doi.org/10.1016/j.icarus.2020.113664>
- Hofgartner, J. D., Hayes, A. G., Campbell, D. B., Lunine, J. I., Black, G. J., MacKenzie, S. M., et al. (2020). The root of anomalously specular reflections from solid surfaces on Saturn's moon Titan. *Nature Communications*, 11(1), 2829. <https://doi.org/10.1038/s41467-020-16663-1>
- Janssen, M. A., Le Gall, A., Lopes, R. M., Lorenz, R. D., Malaska, M. J., Hayes, A. G., et al. (2016). Titan's surface at 2.18-cm wavelength imaged by the Cassini RADAR radiometer: Results and interpretations through the first ten years of observation. *Icarus*, 270, 443–459. <https://doi.org/10.1016/j.icarus.2015.09.027>
- Jaumann, R., Brown, R. H., Stephan, K., Barnes, J. W., Soderblom, L. A., Sotin, C., et al. (2008). Fluvial erosion and post-erosional processes on Titan. *Icarus*, 197(2), 526–538. <https://doi.org/10.1016/j.icarus.2008.06.002>

- Jaumann, R., Kirk, R. L., Lorenz, R. D., Lopes, R. M. C., Stofan, E., Turtle, E. P., et al. (2009). Geology and surface processes on Titan. In R. H. Brown, J.-P. Leberton, & J. H. Waite (Eds.), *Titan from Cassini-Huygens* (pp. 75–140). Springer.
- Karkoschka, E., McEwen, A., & Perry, J. (2017). Producing the best global mosaic of Titan's surface Albedo using Cassini images. *LPSC*, 48, 2518.
- Kirk, R., Howington-Kraus, E., Redding, B., Callahan, P., Hayes, A., Le Gall, A., et al. (2012). Topographic mapping of Titan: Latest results. In *43rd Lunar and Planetary Science Conference, LPI*, (No. 1659, 2759).
- Krasnopolsky, V. A. (2009). A photochemical model of Titan's atmosphere and ionosphere. *Icarus*, 201(1), 226–256. <https://doi.org/10.1016/j.icarus.2008.12.038>
- Langhans, M. H., Jaumann, R., Stephan, K., Brown, R., Buratti, B. J., Clark, R. N., et al. (2012). Titan's fluvial valleys: Morphology, distribution, and spectral properties. *Planetary and Space Science*, 60(1), 34–51. <https://doi.org/10.1016/j.pss.2011.01.020>
- Larsson, R., & McKay, C. P. (2013). Timescale for oceans in the past of Titan. *P&SS*, 78, 22–24. <https://doi.org/10.1016/j.pss.2012.12.001>
- Lavvas, P. P., Coustenis, A., & Vardavas, I. M. (2008). Coupling photochemistry with haze formation in Titan's atmosphere, Part II: Results and validation with Cassini/Huygens data. *Planetary and Space Science*, 56(1), 67–99. <https://doi.org/10.1016/j.pss.2007.05.027>
- Le Mouélic, S., Cornet, T., Rodriguez, S., Sotin, C., Seignovert, B., Barnes, J. W., et al. (2019). The Cassini VIMS archive of Titan: From browse products to global infrared color maps. *Icarus*, 319, 121–132. <https://doi.org/10.1016/j.icarus.2018.09.017>
- Liu, Z. Y. C., Radebaugh, J., Harris, R. A., Christiansen, E. H., Neish, C. D., Kirk, R. L., et al. (2016). The tectonics of Titan: Global structural mapping from Cassini RADAR. *Icarus*, 270, 14–29. <https://doi.org/10.1016/j.icarus.2015.11.021>
- Lopes, R. M., Malaska, M. J., Schoenfeld, A. M., Solomonidou, A., Birch, S. P. D., Florence, M., et al. (2020). A global geomorphologic map of Saturn's moon Titan. *Nature Astronomy*, 4(3), 228–233. <https://doi.org/10.1038/s41550-019-0917-6>
- Lopes, R. M., Mitchell, K. L., Stofan, E. R., Lunine, J. I., Lorenz, R., Paganelli, F., et al. (2007). Cryovolcanic features on Titan's surface as revealed by the Cassini Titan Radar Mapper. *Icarus*, 186, 395–412.
- Lopes, R. M. C., Kirk, R. L., Mitchell, K. L., Le Gall, A., Barnes, J. W., Hayes, A., et al. (2013). Cryovolcanism on Titan: New results from Cassini RADAR and VIMS. *Journal of Geophysical Research: Planets*, 118(3), 1–20. <https://doi.org/10.1002/jgre.20062>
- Lopes, R. M. C., Malaska, M. J., Solomonidou, A., LeGall, A., Janssen, M. A., Neish, C., et al. (2016). Nature, distribution, and origin of Titan's undifferentiated plains (“Blandlands”). *Icarus*, 270, 162–182. <https://doi.org/10.1016/j.icarus.2015.11.034>
- Lopes, R. M. C., Stofan, E. R., Pecyno, R., Radebaugh, J., Mitchell, K. L., Mitri, G., et al. (2010). Distribution and interplay of geologic processes on Titan from Cassini radar data. *Icarus*, 205(2), 540–558. <https://doi.org/10.1016/j.icarus.2009.08.010>
- Lopes, R. M. C., Wall, S. D., Elachi, C., Birch, S. P., Corlies, P., Coustenis, A., et al. (2019). Titan as revealed by the Cassini radar. *Space Science Reviews*, 215(4), 1–50. <https://doi.org/10.1007/s11214-019-0598-6>
- Lorenz, R. D., MacKenzie, S. M., Neish, C. D., Le Gall, A., Turtle, E. P., Barnes, J. W., et al. (2021). Selection and characteristics of the Dragonfly landing site near Selk crater, Titan. *The Planetary Science Journal*, 2(1), 24. <https://doi.org/10.3847/psj/ab008f>
- Lorenz, R. D., Niemann, H. B., Harpold, D. N., Way, S. H., & Zarnecki, J. C. (2006). Titan's damp ground: Constraints on Titan surface thermal properties from the temperature evolution of the Huygens GCMS inlet. *Meteoritics & Planetary Sciences*, 41(11), 1705–1714. <https://doi.org/10.1111/j.1945-5100.2006.tb00446.x>
- Lorenz, R. D., Wall, S., Radebaugh, J., Boubin, G., Reffett, E., Janssen, M., et al. (2006). The sand seas of Titan: Cassini RADAR observations of longitudinal dunes. *Science*, 312(5774), 724–727. <https://doi.org/10.1126/science.1123257>
- Lunine, J. I., Elachi, C., Wall, S. D., Janssen, M., Allison, M. D., Anderson, Y., et al. (2008). Titan's diverse landscapes as evidenced by Cassini RADAR's third and fourth looks at Titan. *Icarus*, 195(1), 415–433. <https://doi.org/10.1016/j.icarus.2007.12.022>
- MacKenzie, S. M., Barnes, J. W., Sotin, C., Soderblom, J. M., Le Mouélic, S., Rodriguez, S., et al. (2014). Evidence of Titan's climate history from evaporite distribution. *Icarus*, 243, 191–207. <https://doi.org/10.1016/j.icarus.2014.08.022>
- Malaska, M. J., & Hodyss, R. (2014). Dissolution of benzene, naphthalene, and biphenyl in a simulated Titan lake. *Icarus*, 242, 74–81. <https://doi.org/10.1016/j.icarus.2014.07.022>
- Malaska, M. J., Lopes, R. M., Hayes, A. G., Radebaugh, J., Lorenz, R., & Turtle, E. (2016). Material transport map of Titan: The fate of dunes. *Icarus*, 270, 183–196. <https://doi.org/10.1016/j.icarus.2015.09.029>
- Malaska, M. J., Lopes, R. M. C., Williams, D. A., Neish, C. D., Solomonidou, A., Soderblom, J. M., et al. (2016). Geomorphological map of the Afekan Crater region, Titan: Terrain relationships in the equatorial and midlatitude regions. *Icarus*, 270, 130–161. <https://doi.org/10.1016/j.icarus.2016.02.021>
- Malaska, M. J., Radebaugh, J., Lopes, R. M. C., Mitchell, K., Verlander, T., Schoenfeld, A., et al. (2020). Labyrinth terrain on Titan. *Icarus*, 344, 113764. <https://doi.org/10.1016/j.icarus.2020.113764>
- Michaelides, R. J., Hayes, A. G., Mastrogiuseppe, M., Zebker, H. A., Farr, T. G., Malaska, M. J., et al. (2016). Constraining the physical properties of Titan's empty lake basins using nadir and off-nadir Cassini RADAR backscatter. *Icarus*, 270, 57–66. <https://doi.org/10.1016/j.icarus.2015.09.043>
- Miller, J. W., Birch, S. P. D., Hayes, A. G., Malaska, M. J., Lopes, R. M. C., Schoenfeld, A. M., et al. (2021). Fluvial features on Titan and Earth: Lessons from planform images in low-resolution SAR. *The Planetary Science Journal*, 2(4), 142. <https://doi.org/10.3847/psj/ac0245>
- Mitri, G., Bland, M. T., Showman, A. P., Radebaugh, J., Stiles, B., Lopes, R. M. C., et al. (2010). Mountains on Titan: Modeling and observations. *Journal of Geophysical Research*, 115(E10), E10002. <https://doi.org/10.1029/2010je003592>
- Mitri, G., Lunine, J. I., Mastrogiuseppe, M., & Poggiali, V. (2019). Possible explosion crater origin of small lake basins with raised rims on Titan. *Nature Geoscience*, 12(10), 791–796. <https://doi.org/10.1038/s41561-019-0429-0>
- Mitri, G., Showman, A. P., Lunine, J. I., & Lopes, R. M. (2008). Resurfacing of Titan by ammonia-water cryomagma. *Icarus*, 196(1), 216–224. <https://doi.org/10.1016/j.icarus.2008.02.024>
- Mitri, G., Showman, A. P., Lunine, J. I., & Lorenz, R. D. (2007). Hydrocarbon lakes on Titan. *Icarus*, 186(2), 385–394. <https://doi.org/10.1016/j.icarus.2006.09.004>
- Moore, J. M., & Howard, A. D. (2010). Are the basins of Titan's Hotei Regio and Tui Regio sites of former low latitude seas? *Geophysical Research Letters*, 37(22), L22205. <https://doi.org/10.1029/2010gl0145234>
- Moore, J. M., Howard, A. D., & Morgan, A. M. (2014). The landscape of Titan as witness to its climate evolution. *Journal of Geophysical Research: Planets*, 119(9), 2060–2077. <https://doi.org/10.1002/2014JE004608>
- Neish, C. D., Barnes, J. W., Sotin, C., MacKenzie, S., Soderblom, J. M., Le Mouélic, S., et al. (2015). Spectral properties of Titan's impact craters imply chemical weathering of its surface. *Geophysical Research Letters*, 42(10), 3746–3754. <https://doi.org/10.1002/2015gl03824>
- Neish, C. D., Kirk, R. L., Lorenz, R. D., Bray, V. J., Schenk, P., Stiles, B. W., et al. (2013). Crater topography on Titan: Implications for landscape evolution. *Icarus*, 223(1), 82–90. <https://doi.org/10.1016/j.icarus.2012.11.030>
- Neish, C. D., & Lorenz, R. D. (2012). Titan's global crater population: A new assessment. *Planetary and Space Science*, 60(1), 26–33. <https://doi.org/10.1016/j.pss.2011.02.016>

- Neish, C. D., Molaro, J. L., Lora, J. M., Howard, A. D., Kirk, R. L., Schenk, P., et al. (2016). Fluvial erosion as a mechanism for crater modification on Titan. *Icarus*, 270, 114–129. <https://doi.org/10.1016/j.icarus.2015.07.022>
- Nelson, R. M., Kamp, L. W., Lopes, R. M. C., Matson, D. L., Kirk, R. L., Hapke, B. W., et al. (2009). Photometric changes on Saturn's Moon Titan: Evidence for cryovolcanism. *Geophysical Research Letters*, 36(4), L04202. <https://doi.org/10.1029/2008GL036206>
- Poggiali, V., Mastrogioiuseppe, M., Hayes, A., Seu, R., Birch, S., Lorenz, R., et al. (2016). Liquid-filled canyons on Titan. *Geophysical Research Letters*, 43(15), 7887–7894. <https://doi.org/10.1002/2016gl069679>
- Radebaugh, J., Lorenz, R. D., Kirk, R. L., Lunine, J. I., Stofan, E. R., Lopes, R. M. C., & Wall, S. D. (2007). Mountains on Titan as observed by Cassini radar. *Icarus*, 192(1), 77–91. <https://doi.org/10.1016/j.icarus.2007.026.020>
- Radebaugh, J., Lorenz, R. D., Lunine, J. I., Wall, S. D., Boubin, G., Reffet, E., et al. (2008). Dunes on Titan observed by Cassini radar. *Icarus*, 194(2), 690–703. <https://doi.org/10.1016/j.icarus.2007.10.015>
- Radebaugh, J., Lorenz, R. D., Wall, S. D., Kirk, R. L., Wood, C. A., Lunine, J. I., et al. (2011). Regional geomorphology and history of Titan's Xanadu province. *Icarus*, 211(1), 672–685. <https://doi.org/10.1016/j.icarus.2010.07.022>
- Radebaugh, J., Ventra, D., Lorenz, R. D., Farr, T. G., Kirk, R. L., Hayes, A., et al. (2018). Alluvial and fluvial fans on Saturn's Moon Titan reveal processes, materials and regional geology. In D. Ventra & L. E. Clarke (Eds.), *Geology and geomorphology of alluvial and fluvial fans: Terrestrial and planetary perspectives* (p. 440). Geological Society, London, Special Publications.
- Rodriguez, S., Garcia, A., Lucas, A., Appéré, T., Le Gall, A., Reffet, E., et al. (2014). Global mapping and characterization of Titan's dune fields with Cassini: Correlation between RADAR and VIMS observations. *Icarus*, 230, 168–179. <https://doi.org/10.1016/j.icarus.2013.11.017>
- Rodriguez, S., Vinatier, S., Cordier, D., Tobie, G., Achterberg, R. K., Anderson, C. M., et al. (2022). Science goals and new mission concepts for future exploration of Titan's atmosphere, geology and habitability: Titan Polar scout/orbitEr and in situ lake lander and DrONE explorer (POSEIDON). *Experimental Astronomy*, 1–63. <https://doi.org/10.1007/s10686-021-09815-8>
- Schoenfeld, A. (2022). Soi crater region mapping shapefiles. Mendeley Data V1. <https://doi.org/10.17632/z4jvkvr25b.1>
- Schoenfeld, A., Lopes, R., Malaska, M., Solomonidou, A., Williams, D., Birch, S., et al. (2021). Geomorphological map of the South Belet region of Titan. *Icarus*, 366, 114516. <https://doi.org/10.1016/j.icarus.2021.114516>
- Seignovert, B., Le Mouelic, S., Brown, R. H., Joseph, E., Karkoschka, E., Pasek, V., et al. (2019). Titan's global map combining VIMS and ISS mosaics. *EPSC, 2019*, EPSC-DPS2019.
- Soderblom, L. A., Kirk, R. L., Lunine, J. I., Anderson, J. A., Baines, K. H., Barnes, J. W., et al. (2007). Correlations between Cassini VIMS spectra and RADAR SAR images: Implications for Titan's surface composition and the character of the Huygens Probe Landing Site. *Planetary and Space Science*, 55(13), 2025–2036. <https://doi.org/10.1016/j.pss.2007.04.014>
- Sohl, F., Solomonidou, A., Wagner, F. W., Coustenis, A., Hussmann, H., & Schulze-Makuch, D. (2014). Tidal stresses on Titan and implications for its geology and habitability. *Journal of Geophysical Research: Planets*, 119(5), 1013–1036. <https://doi.org/10.1002/2013je0004512>
- Solomonidou, A., Bampasidis, G., Hirtzig, M., Coustenis, A., Kyriakopoulos, K., Seymour, K. S., et al. (2013). Morphotectonic features on Titan and their possible origin. *Planetary and Space Science*, 77, 104–117. <https://doi.org/10.1016/j.pss.2012.05.003>
- Solomonidou, A., Coustenis, A., Hirtzig, M., Rodriguez, S., Stephan, K., Lopes, R. M. C., et al. (2016). Temporal variations of Titan's surface with Cassini/VIMS. *Icarus*, 270, 85–99. <https://doi.org/10.1016/j.icarus.2015.05.003>
- Solomonidou, A., Coustenis, A., Lopes, R. M., Malaska, M. J., Rodriguez, S., Drossart, P., et al. (2018). The spectral nature of Titan's major geomorphological units: Constraints on surface composition. *Journal of Geophysical Research: Planets*, 123(2), 489–507. <https://doi.org/10.1002/2017je005477>
- Solomonidou, A., Le Gall, A., Malaska, M. J., Birch, S. P. D., Lopes, R. M. C., Coustenis, A., et al. (2020). Spectral and emissivity analysis of the raised ramparts around Titan's northern lakes. *Icarus*, 344, 113338. <https://doi.org/10.1016/j.icarus.2019.05.040>
- Solomonidou, A., Neish, C., Coustenis, A., Malaska, M., Le Gall, A., Lopes, R., et al. (2020). The chemical composition of impact craters on Titan I. Implications for exogenic processing. *Astronomy & Astrophysics*, 641, A16. <https://doi.org/10.1051/0004-6361/202037866>
- Stiles, B. W. (2017a). Cassini orbiter SSA RADAR 5 BIDR V1.0. Planetary Data System V1. <https://doi.org/10.17189/1520231>
- Stiles, B. W. (2017b). Cassini orbiter SSA RADAR 5 STDR V1.0. Planetary Data System V1. <https://doi.org/10.17189/1520238>
- Stiles, B. W., Gim, Y., Hamilton, G., Hensley, S., Johnson, W. T., Shimada, J., et al. (2006). Ground processing of Cassini RADAR imagery of Titan. In *2006 IEEE Conference on Radar* (p. 8). IEEE.
- Stiles, B. W., Hensley, S., Gim, Y., Bates, D. M., Kirk, R. L., Hayes, A., et al. (2009). Determining Titan surface topography from Cassini SAR data. *Icarus*, 202(2), 584–598. <https://doi.org/10.1016/j.icarus.2009.03.032>
- Stofan, E. R., Elachi, C., Lunine, J. I., Lorenz, R. D., Stiles, B., Mitchell, K. L., et al. (2007). The lakes of Titan. *Nature*, 445(7123), 61–64. <https://doi.org/10.1038/nature05438>
- Stofan, E. R., Lunine, J. I., Lopes, R., Paganelli, F., Lorenz, R. D., Wood, C. A., et al. (2006). Mapping of Titan: Results from the first Two Titan radar passes. *Icarus*, 185, 443–456. <https://doi.org/10.1016/j.icarus.2006.07.015>
- Sulaiman, A. H., Achilleos, N., Bertucci, C., Coates, A., Dougherty, M., Hadid, L., et al. (2021). Enceladus and Titan: Emerging worlds of the Solar System. *Experimental Astronomy*, 1–28. <https://doi.org/10.1007/s10686-021-09810-z>
- Tobie, G., Teanby, N. A., Coustenis, A., Jaumann, R., Raulin, F., Schmidt, J., et al. (2014). Science goals and mission concept for the future exploration of Titan and Enceladus. *Planetary and Space Science*, 104, 59–77. <https://doi.org/10.1016/j.pss.2014.10.002>
- Turtle, E. P., Del Genio, A. D., Barbara, J. M., Perry, J. E., Schaller, E. L., McEwen, A. S., et al. (2011). Seasonal changes in Titan's meteorology. *Geophysical Research Letters*, 38(3), L03203. <https://doi.org/10.1029/2010gl046266>
- Turtle, E. P., Perry, J. E., McEwen, A. S., Del Genio, A. D., Barbara, J., West, R. A., et al. (2009). Cassini imaging of Titan's high-latitude lakes, clouds, and south-polar surface changes. *Geophysical Research Letters*, 36(2), L02204. <https://doi.org/10.1029/2008gl036186>
- Wall, S. D., Lopes, R. M., Stofan, E. R., Wood, C. A., Radebaugh, J. L., Hörst, S. M., et al. (2009). Cassini RADAR images at Hotei Arcus and western Xanadu, Titan: Evidence for geologically recent cryovolcanic activity. *Geophysical Research Letters*, 36(4), L04203. <https://doi.org/10.1029/2008gl036415>
- Werynski, A., Neish, C. D., Le Gall, A., & Janssen, M. A., & The Cassini RADAR Team. (2019). Compositional variations of Titan's impact craters indicates active surface erosion. *Icarus*, 321, 508–521. <https://doi.org/10.1016/j.icarus.2018.12.007>
- Williams, D. A., Radebaugh, J., Lopes, R. M. C., & Stofan, E. (2011). Geomorphologic mapping of the Menrva region of Titan using Cassini RADAR data. *Icarus*, 212(2), 744–750. <https://doi.org/10.1016/j.icarus.2011.01.014>
- Wilson, E. H., & Atreya, S. K. (2004). Current state of modeling the photochemistry of Titan's mutually dependent atmosphere and ionosphere. *Journal of Geophysical Research*, 109(E6), E06002. <https://doi.org/10.1029/2003JE002181>
- Wood, C. A., Lorenz, R., Kirk, R., Lopes, R., Mitchell, K., & Stofan, E., & The Cassini RADAR Team. (2010). Impact craters on Titan. *Icarus*, 206(1), 334–344. <https://doi.org/10.1016/j.icarus.2009.08.021>